BRITTLE-TO-DUCTILE TRANSITION IN NiAl SINGLE CRYSTALS

By

SANJAY SHRIVASTAVA

A DISSERTATION PRESENTED TO THE GRADUATE SCHOOL
OF THE UNIVERSITY OF FLORIDA IN PARTIAL FULFILLMENT
OF THE REQUIREMENTS FOR THE DEGREE OF
DOCTOR OF PHILOSOPHY

UNIVERSITY OF FLORIDA

1997

TO MY PARENTS

iii

Swanson and Debbie Hall in the academic records office, April and Julie in the finance office, and Wayne Acree in MAIC for making my life easier. Financial support during this study from the Air Force Office of Scientific Research (URI Grant No. F49620-93-1-030) is gratefully acknowledged.

Last but not the least, I am specially thankful to my parents and elder brother who have been a constant source of inspiration.

TABLE OF CONTENTS

Abstract of Dissertation Presented to the Graduate School
of the University of Florida in Partial Fulfillment of the
Requirements for the Degree of Doctor of Philosophy

BRITTLE-TO-DUCTILE TRANSITION IN NIAL SINGLE CRYSTALS

By

Sanjay Shrivastava

May 1997

Chairperson: Prof. Fereshteh Ebrahimi
Major Department: Materials Science and Engineering

NiAl is a potential candidate for high temperature structural applications because

of its high melting point, high thermal conductivity, relatively low density, and good high

temperature oxidation resistance. However, it suffers from a high brittle-to-ductile

transition (BDT) temperature and a low room temperature toughness. The present study

focuses on understanding the mechanism of the BDT and investigating the effects of

strain rate and prestraining on the BDT in stoichiometric NiAl single crystals.

The results of this study indicated that the BDT temperature (BDTT) correlates

with the onset of net-section yielding in the double-notched tension specimens. A strong

dependence of the BDTT on the applied displacement rate was observed. It was proposed

that the BDT arises from a reduction in strain hardening rate as well as in yield strength

with temperature. The similarity found in activation energy values calculated based on

the strain rate dependence of fracture toughness and tensile data supports this proposal.

While the prestraining was found to increase the toughness at room temperature nearly two-fold, it also increases the BDTT of NiAl single crystals. This observation suggested that the BDT of NiAl is not limited by the dislocation density. Based on the fractographic analysis, it was found that localization of strain is responsible for crack nucleation in NiAl single crystals. It was suggested that the crack instability is "nucleation-controlled" at low temperatures whereas it is "propagation-controlled" at high temperatures. Based on this suggestion, the increase in room temperature toughness upon prestraining was attributed to the reduction in the localization of strain upon prestraining achieved due to the enhanced dislocation density. The increase in the BDTT upon prestraining was attributed to the increased yield stress caused due to prestraining.

The cleavage plane for NiAl single crystals was found to be {511} for the specimen geometry and orientation used in the study. The observation of this cleavage plane is in agreement with the previously reported results. The cleavage plane was independent of heat-treatment, prestraining, and temperature; however, the size of the largest cleavage facet was found to decrease with increasing temperature.

INTRODUCTION

The intermetallic compound NiAl possesses a high melting temperature (1911K), high thermal conductivity (four to eight times that of Ni-based superalloys), relatively low density (two thirds of the conventional Ni-based superalloys) and good high temperature oxidation resistance. The low density of NiAl provides one of the major benefits of NiAl for aircraft engine applications. The decreased density results in lower self induced stresses in rotating turbine airfoils, and the turbine disks may be down-sized to reflect the lower operating stresses imposed by the reduced mass of the blades. The total reduction in weight for the turbine rotor stage (blades plus disk) is projected to range 30-40%. Besides the advantage of the low density, an equally important payoff comes from the high thermal conductivity of NiAl. The high thermal conductivity provides an improved cooling efficiency. These properties make it a potential candidate for high temperature structural applications.[1-7] Besides the above mentioned advantages, for NiAl to be a successful high temperature structural material, a good combination of high-temperature strength and room temperature ductility and fracture toughness is required. However, stoichiometric NiAl suffers from low room temperature ductility and fracture toughness.[8-12]

        The tensile ductility of NiAl has been studied by many investigators[13-15]. However, there has been very limited work on improving its fracture toughness. Most materials undergo a brittle-to-ductile transition (BDT) as the temperature is increased. One way of enhancing the room temperature toughness may be by decreasing the brittle-to-ductile transition temperature (BDTT) to below room temperature. In order to reduce the BDTT, it is imperative to understand the mechanism and the nature of the BDT. In steels and several other metals and alloys, this transition occurs below room temperature. However, in many other materials, this transition occurs at relatively high temperatures (such as for Si the BDT occurs at about 1000K)[16]. The term "brittle-to-ductile transition temperature" can be defined in several different ways. Historically, the term was used to describe the temperature regime where the Charpy V-notch impact energy of steels changed drastically. In steels, the BDT is associated with a change in fracture morphology. Steels exhibit a brittle fracture by cleavage mode below the BDTT and a ductile fracture by micro-void coalescence above the BDTT. In the case of brittle materials such as Si and Al_2O_3, the BDTT is defined as the temperature above which plasticity precedes fracture in toughness tests. In silicon, the BDT is associated with dislocation generation at the crack tip, i.e., below the BDT, there is no dislocation generation at the crack tip and above the BDT, dislocations are generated at the crack tip leading to crack tip plasticity. Silicon has a partial covalent bonding and a very high Peierls stress. As a result, it is very difficult to generate dislocations in single-crystalline silicon. These factors contribute to a high BDTT in silicon.

NiAl has been suggested to have a strong covalent bond between nearest neighbor Ni and Al atoms and a weak ionic repulsion between second-nearest neighbor atoms along <100>, and these bonds are superimposed by a metallic bond[17]. When compared to a semi-brittle bcc metal such as Mo, NiAl has a comparable lower-shelf fracture toughness (4-12 MPam$^{1/2}$) but its BDTT is much higher (Mo$_{[100]}$: BDTT/T$_m$=0.05-0.07; NiAl: BDTT/T$_m$=0.26). This difference in BDTT can not be attributed to a difference in yield strength since NiAl is softer than Mo (σ_{ys} of Mo$_{[100]}$=160 MPa; σ_{ys} of NiAl$_{[110]}$=100 MPa)[18,19]. The surface energy values reported for the {110} cleavage in NiAl are somewhat smaller than the value reported for the {100} cleavage for Mo (Mo: 1.96J/m^2, NiAl: 1.7 J/m^2)[18,19]. The BDT is a result of two competing processes, viz., crack tip plasticity and cleavage. Based on the above comparison with Mo, NiAl has an ease in both the processes, viz., plastic flow and cleavage, which suggests that either NiAl is inherently brittle or stresses become easily localized in this material.

The present study focuses on the BDT phenomenon in NiAl single crystals. The single-crystalline NiAl was chosen for the study as opposed to the more conventional poly-crystalline material for three reasons: (i) single-crystalline NiAl has more technological importance due to its better creep properties, (ii) single-crystalline material provides a better understanding of atomic level phenomena occurring in materials, (iii) polycrystalline NiAl fractures predominantly in an intergranular manner. The objectives of this study include establishing the BDTT and understanding the mechanisms responsible for the BDT in NiAl single crystals. In order to get an insight into the mechanism of the BDT, it was necessary to investigate the effects of displacement rate

and enhanced dislocation density on the BDTT and also to understand the crack nucleation and propagation mechanisms in NiAl single crystals.

The approach taken in this study involved conducting fracture toughness tests over a range of temperatures and displacement rates. Tensile properties such as the yield strength, strain hardening exponent, and ductility as a function of strain rate and temperature were also evaluated for the same geometry and orientation of specimens as used for the toughness testing. In order to establish if the BDT of NiAl single crystals is limited by the dislocation density, it was also necessary to study the toughness and BDT behavior of the prestrained specimens. This required establishing a prestraining procedure and conducting toughness tests over a range of temperature for the prestrained specimens. Fracture surfaces and crack profiles of the tested specimens were analyzed to study the effect of test conditions on crack nucleation and propagation. The experimental data were used to determine the activation energy associated with the thermally activated deformation using a model proposed by Reed-Hill et al.[20] The activation energy of the BDT was compared with the activation energy of thermally activated deformation.

CHAPTER 2
LITERATURE REVIEW

This chapter comprises of three sections. In the first section, the existing

literature on the properties of NiAl with an emphasis on mechanical properties has been

reviewed. The second section deals with the fundamentals of fracture mechanics relevant

to the present study. In the third section, the existing theories and models of the BDT

have been reviewed.

2.1 Properties of NiAl

2.1.1 Crystal Structure and Phase Stability

NiAl has a B2 crystal structure similar to the body-centered-cubic (BCC) structure

which comprises of two interpenetrating simple cubic cells where Ni atoms occupy the

corners of one cubic cell and Al atoms occupy the corners of the other cubic cell[2]. The

crystal structure of NiAl is shown in Figure 2.1. The Ni-Al binary phase diagram is

shown in Figure 2.2[2]. The phase diagram shows that the intermetallic compound NiAl

has a very high melting point of 1911K. This compound also has a wide phase field

ranging from 45 atom% to 59 atom% Ni.
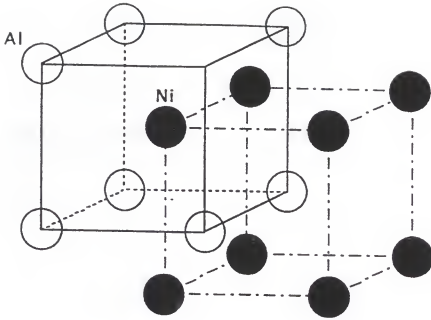
Figure 2.1 Crystal structure of NiAl[2].
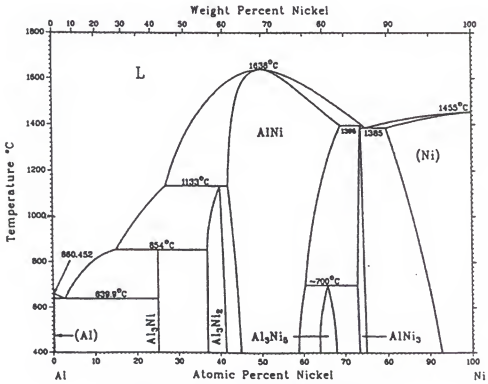
Figure 2.2 Ni-Al binary phase diagram[2].

2.1.2 Slip and Flow Behavior

In NiAl, the shortest translation vector that will maintain the B2 structure is that along the cube edge (i.e., in the <001> crystallographic direction)[20-22]. NiAl single crystals exhibit two different types of slip behavior depending upon crystal orientation. For single crystals in "soft" orientations and in polycrystals, the dominant slip vector is <001>[23-28]. In addition, it has been observed that NiAl in soft orientations deforms by <001> slip on either the {100} or the {110} slip planes in accordance with Schmid's law[23-28]. If the loading direction is along <001>, the "hard" orientation, the resolved shear stress along <001> directions has a near zero value resulting in the operation of alternative slip systems at very large yield stresses. The operative slip vector is <111> at low and intermediate temperatures, and is a combination of <011> and <001> at elevated temperatures[20-22]. Table 2.1 lists the slip systems observed at different temperatures in NiAl[3].

In fracture toughness tests, stresses in the vicinity of the crack tip are extremely high. The presence of extremely high stresses near the notch tip in fracture toughness tests may cause deviations from the slip behavior observed during the tensile testing. Recent analysis[29] of the crack tip stress field in NiAl single crystals for a crack propagating in the [101] direction on the (010) plane has revealed that only one of the three {110}<001> slip systems was capable of sustaining considerable plastic flow. This analysis also showed that other possible slip systems such as {110}<111> and {112}<111> may be activated over regions extremely close to the crack tip.

Similar to BCC transition metals, the yield stress of NiAl is sensitive to temperature. The yield stress exhibits a strong temperature dependence at low temperatures and a plateau at intermediate temperatures where only a mild temperature dependence of yield stress is observed.[30-33] The temperature dependence of yield stress is shown in Figure 2.3 for different orientations.

Table 2.1: Observed slip systems in uniaxially deformed NiAl[3].

Material	Temperature Range, (K)	Slip Vector	Slip Plane	Analysis Technique[a, b]
Polycrystalline NiAl	300-900	<100>	{001}	TEM
Single Crystal NiAl "Soft" Orientations:				
	77-1373	<100>	{011}	SSTA/TEM
[111]	77-300	<100>	{011}	SSTA
[122]	77-873	<100>	{011}	TEM
[123]	77-300	<100>	{011}	SSTA/TEM
[110]	300-1373	<100>	{011}	SSTA/TEM
[110]	573	<100>	{011}	SSTA
[227]	77-873	<100>	{011} or {001}	SSTA/TEM
[112]				
"Hard" Orientation:				
[001]	300-1300	<100>	{011}	SSTA/TEM
	600-1372	<110>	{011}	SSTA/TEM
	77-600	<111>	{112}, {011}, or {123}	SSTA/TEM

[a] TEM - Transmission Electron Microscopy Investigation
[b] SSTA - Surface Slip Trace Analysis
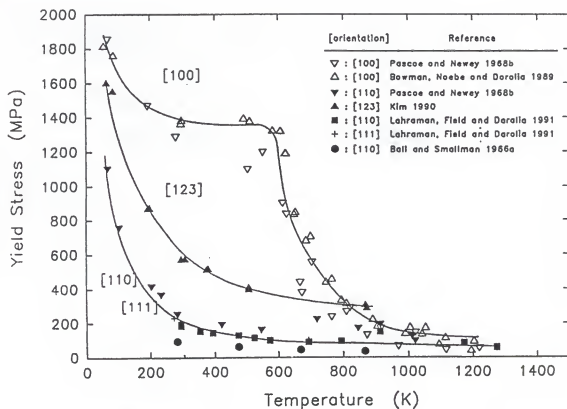
Figure 2.3 Yield strength of NiAl single crystals for different orientations as a function of temperature[3].

2.1.3 Ductility, Fracture Toughness And Fracture Path

The ductility of polycrystalline NiAl is practically zero at room temperature. Soft oriented NiAl single crystals show ductilties in the range of 1-5%. Higher room temperature ductilities have been achieved using various schemes such as heat treatment, microalloying, and prestraining[7]. Levit, Kaufman and coworkers[13] have observed tensile elongation as high as 35% at room temperature by carefully selecting the specimen orientation and geometry. While high tensile elongations have been achieved, there has been very limited work on the enhancing fracture toughness of NiAl single crystals.

Room temperature fracture toughness of NiAl has been reported to be in the range of 7 to 11 $MPam^{1/2}$ when the notch plane is {001} and 4 to 7 $MPam^{1/2}$ when the notch plane is {011}[8-11]. Chang, Darolia and Lipsitt[8] performed single-edge-notched four point bend (SENB) tests at a loading rate of 9μm/sec and reported room temperature toughness values in the range of 7.3 to 9.3 $MPam^{1/2}$ when the notch plane was {001}, and between 3.8 and 5.1 $MPam^{1/2}$ when the notch plane was {011}. The anisotropy in toughness was attributed to the difference in crack path. Bergmann and Vehoff[10] reported toughness values of 11 and 5 $MPam^{1/2}$ for the two orientations, respectively. The loading rate used in their study was 0.2μm/sec. They also measured toughness in a fatigue pre-cracked specimen and reported values that were slightly lower than the notched specimen.

The fracture path for the two orientations has been analyzed by Chang et al[8]. In their study, the specimens oriented with {011} as the notch plane fractured macroscopically along {011} planes in SENB bend tests. The specimens oriented with

{001} as the notch plane showed {511} fracture facets when tested in SENB tests. In specimens tested with a chevron-notch, the fracture path is constrained to the plane of the notch.

The fracture surfaces of tensile specimens were analyzed by Schneibel et al[34]. They did not observe any preferred {011} cleavage. They occasionally found facets close to {511} and {711} planes. For the <011> orientation, fracture tended to occur at 45^0 angle to the tensile axis (i.e., in the direction of maximum shear stress). In the case of the <111> orientation fracture facets exhibited similar angles but were, at the same time, close to {011} planes. In a <001> specimen, the fracture surface normals tended to include an angle close to 35^0 with the tensile axis.

Very little is known about the BDT in NiAl. In a preliminary investigation, Bergmann and Vehoff[10] reported that fracture toughness increased from 5 MPam$^{1/2}$ at room temperature to 12 MPam$^{1/2}$ at 200^0C for the specimen with the notch plane oriented to be {011} and increased from 11 MPam$^{1/2}$ at room temperature to 35 MPam$^{1/2}$ at 275^0C for the specimen with the notch plane oriented to be {001}. The BDT as characterized by tensile elongations was determined to be in the range of 200^0C to 250^0C for the specimens having the {011} tensile axis and 325^0C for the specimens having the {001} tensile axis[6,30]. However, there had been no study to determine the mechanism of the BDT in NiAl single crystals. It was not known whether the BDTT in NiAl single crystals is strain rate dependent.

2.1.4 Effect of Point Defects on Mechanical Properties

The initial dislocation density of NiAl single crystals is rather low[35]. Moreover, these dislocations could be locked in by solute atmospheres and by other point defects and larger defects, a phenomenon similar to strain aging in BCC metals. The possible scenarios include pinning of dislocations by point defects, viz. interstitial atoms, substitutional atoms, and vacancies as well as by larger defects such as voids, jogs, and precipitates. The degree of pinning can be controlled by heat treatment and cooling rate.

NiAl possesses relatively large number of thermal vacancies owing to the very low energy of thermal vacancy formation associated with NiAl[36]. These vacancies interact with dislocations and provide hardening. The hardening due to vacancies could be a result of one or more of the following interactions: (i) the strain field of vacancies can interact with that of the dislocations and make them immobile, (ii) vacancies can form voids and voids of optimum size can pin dislocations, (iii) vacancies can form jogs on dislocations which impede the motion of dislocations.

In an earlier study[37], these vacancies were reported to form voids upon heat treating in the temperature range of 973-1173K. The nucleation of these voids was suggested to occur by the formation of vacancy/impurity complexes. The same researchers subsequently showed that the presence of a small amount of carbon increases the density of these voids[38]. In more recent studies by two independent groups, void formation was reported to occur at 673K and 800K[39,40]. In another study by Epperson et al.[41], similar voids were observed upon annealing NiAl single crystals in the temperature range of 673-1573K.

In addition, the dependence of mechanical properties of NiAl on stoichiometry is indicative of the role of constitutional vacancies and their interactions with other defects. Vedula and Khadkikar[42] have shown that the yield strength shows a minimum at the stoichiometric composition. This behavior has been attributed to the increased concentration of constitutional vacancies upon deviating from the stoichiometric composition. Lim et al.[43] reported the effect of constitutional vacancies by measuring changes in resistivity in off-stoichiometric NiAl. In a more recent study by Duncan and Kaufman,[44] the hardening behavior of NiAl has been attributed to increased vacancy concentration and a resulting enhanced interaction with other defects.

Segregation of interstitial solutes to dislocation cores is a well known phenomenon occurring in several materials. The sensitivity of the fracture toughness of NiAl single crystals to heat treatment and cooling rate is indicative of the occurrence of interstitial segregation to dislocation cores in NiAl single crystals[9]. Solute atoms tend to segregate to dislocations at intermediate temperatures if they are given enough time to diffuse to dislocations. At lower temperatures, solute atoms do not have enough mobility, whereas at higher temperatures, solute atoms have an energy level higher than the binding energy of dislocation/solute. Thus, the pinning of solutes to dislocations can be controlled by controlling the cooling rate in the intermediate temperature regime. Vacancy concentration and void formation can be controlled by the heat treatment and cooling rates in the higher temperature regime.

The effect of point defects on the mechanical properties of NiAl has also been shown by static and dynamic strain aging. The occurrences of static and dynamic strain

aging manifested by the appearance of the yield point, serrations, and by a negative strain rate sensitivity have been reported in NiAl[45].

2.2 Principles of Fracture Mechanics

The discrepancy between the observed fracture strength of crystals and the theoretical cohesive strength led to the proposition of stress concentration due to the presence of fine cracks in a solid by Griffith[46] in 1920. Griffith's criterion for the propagation of a crack was based on the release of the stored elastic energy. Later, Inglis[47] proposed a mathematical solution to the stress distribution for an elliptical crack. Irwin[48] followed the work done by Griffith, Orowan, and Inglis and developed linear elastic fracture mechanics. Based on a solution proposed by Westergaard[49] for a sharp crack loaded in mode I, Irwin[48] derived the following for an infinite plate loaded under uniaxial stresses:

$$K_I = c\sigma\sqrt{a}$$

where σ is the applied stress, a is the crack size, and c is a geometric parameter which depends on the crack size, geometry, and the specimen geometry. Mathematical expressions using finite element and other methods have been developed determining the geometric parameter for a number of crack and specimen geometries and are available in the literature. Under plane strain or plane stress conditions, K_I is known as the stress intensity factor. The stress intensity factor, K_I, is then a measure for the stress singularity

at the crack tip. A critical value of K_I called K_{IC} is termed as the fracture toughness and is considered to be a material property. It describes the inherent resistance of the material to failure in the presence of a stress concentrators (such as cracks, sharp corners). K_{IC} is valid for materials where there is no yielding or a small scale yielding.

Another parameter which characterizes the fracture toughness of more ductile materials is called the J integral. Rice[50] showed that the line integral related to the energy in the vicinity of a crack can be used to solve two-dimensional crack problems in the presence of plastic deformation. Fracture occurs when the J integral reaches a critical value. In the case of small scale yielding, J becomes equal to the crack driving force.

Due to the stress concentration ahead of a crack, stresses in the vicinity of the crack are very high. There is a zone around the crack tip where the stresses are higher than the stress needed for the yielding of the material, this zone is termed as the "plastic zone" in elastic-plastic solids. Several approaches have been made to estimate the plastic zone sizes of materials, the most common expression for estimating the plastic zone size relates the plastic zone size with the yield stress and the fracture toughness of a material[51]. Under the plane strain conditions, it is given by the equation below:

$$r_Y = \frac{1}{6\pi} \left(\frac{K_I}{\sigma_Y} \right)^2 \tag{2.2}$$

where r_Y is the plastic zone size, σ_Y is the yield stress, and K_I is the applied stress intensity factor. The plastic zone size is larger under the plane stress conditions.
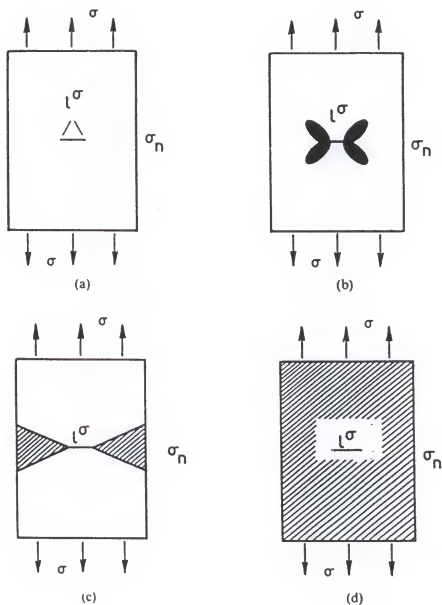
Figure 2.4 Schematics showing different degrees of yielding (a) LEFM, (b) small scale yielding, (c) net-section yielding, (d) general yielding[52].

Figure 2.4 shows the schematic representation of increasing degrees of yielding[52]. This figure shows four different levels of yielding. In the first case, the yielding is limited to a zone in the immediate vicinity of the crack. This zone is vanishingly small and the case is termed as Linear Elastic Fracture Mechanics (LEFM). In the second case, the yielding is extensive, but does not spread to the lateral boundary of the structure and is thus contained. This is a regime which can be called elastic-plastic and to which yielding fracture mechanics can be applied, but for which LEFM, with correction for the extent of the plastic zone, may still give an acceptable answer. The third case involves an extensive yielding which spreads to the boundary ahead of the crack, and is thus uncontained. This regime can be called net-section yield, to which yielding fracture mechanics must be applied. For configurations with little lateral constraint and low hardening, tough materials may fail by plastic collapse of the net-section, whilst for less tough materials a crack may spread by stable or unstable growth. The fourth case occurs when the applied stress is greater than the yield stress, extensive plasticity develops along the components as well as across the section, implying work hardening of the net section. This regime can be called general yield.

Under several conditions, a distribution of microcracks of varying sizes may be present in a material. Then, under an applied loading, these microcracks grow, and constantly change their size, which, in turn, changes the stress intensity factor and change in stress intensity factor, again, changes the growth rate of different microcracks. Thus, a dynamic condition prevails. Curry and Knott[53] have developed formulations for the probability of fracture when there is a distribution of microcracks present. Their

formulation was based on quenched and tempered steels where the cracks originated by the fracture of carbide particles. Curry and Knott[53] studied the distribution of carbide particles and used this distribution to predict the cleavage fracture toughness of steels. This model can be used for the prediction of fracture toughness when there is a distribution of microcracks present in the material.

2.3 Theories of the BDT

The temperature dependence of K_{IC} has been modeled in a quantitative way for steels[54]. The stress distribution ahead of a sharp crack based on a model proposed by Rice and Johnson[55] is shown in Figure 2.5 (a). The simplest fracture criterion is based on achieving a maximum principal stress, σ_{yy}, equal to the fracture stress, σ_f, ahead of the notch. However, σ_f is largely independent of temperature[54], therefore, the temperature dependence of K_{IC} could not be modeled based upon the fracture stress criterion alone. It was postulated that the temperature dependence of K_{IC} is determined by the requirement that the maximum principal stress, σ_{yy}, at the crack tip equals or exceeds this critical value over a microstructurally significant size scale. In Figure 2.5 (a), the stress intensification ratio R (ratio of the tensile stress σ_{yy} to the flow stress σ_0) is plotted against the dimensionless quantity $X/(K/\sigma_0)^2$, where X is the coordinate of a material point before deformation, and K is the stress intensity factor for a non-hardening material under conditions of small scale yielding. In Figure 2.5 (b), the stress distribution based on the singularity solution for a strain hardening material derived by Hutchinson[56], and Rice and Rosengren[57].
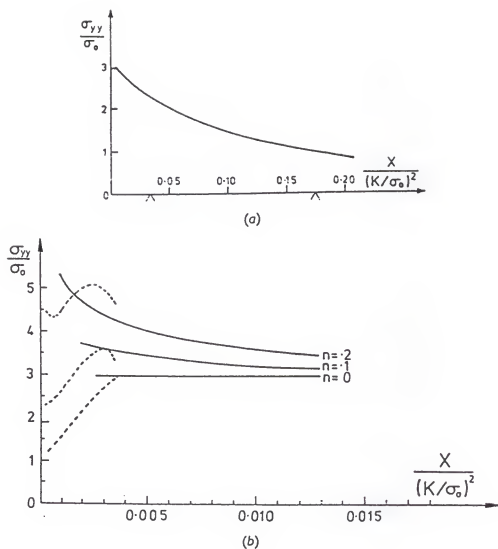
Figure 2.5 (a) Stress distribution for small scale yielding condition for a non-hardening material. (b) Stress distribution due to crack tip blunting for materials with various strain hardening components[54].

At low temperatures, little stress intensification is needed since σ_0 is high and the critical fracture stress can be met by a point on Figure 2.5 (a) not too far behind the plastic-elastic interface. The absolute size of the plastic zone for a given value of K is small because the yield stress is high. As the temperature is raised, increasing stress intensification is required, which now involves work hardening as well as constraint, because the strains in the plastic zone become significant. Hence, the failure point is now found on the Power hardening curve (Figure 2.5 b) and moves progressively closer to the maximum in the curve as the temperature is raised. It is clear from this figure that the stress distribution also depends on the strain hardening behavior. If the strain hardening rate is high, the stress values are higher near the notch tip.

The BDT in single crystals is related to the formation and growth of a plastic zone around the crack tip. At and above the BDT, plastic processes blunt and shield the crack tip. Plasticity can occur by nucleation of dislocations at the crack tip or by motion and multiplication of the existing dislocations in the crystals near the crack tip. Based upon this, the BDTT in different single crystals is either dislocation nucleation/multiplication-controlled or dislocation-mobility controlled[58-62]. The BDTT in some materials is strongly dependent on the strain rate. This strong strain rate dependence of the BDTT may suggest a dislocation mobility controlled BDTT.

Materials can be classified into two classes based upon the shape of their brittle-to-ductile-transition. Materials with low dislocation density such as silicon and alumina have been known to exhibit a sharp BDT [Figure 2.6 (a)] and materials with a relatively high dislocation density such as molybdenum and titanium aluminides have been known
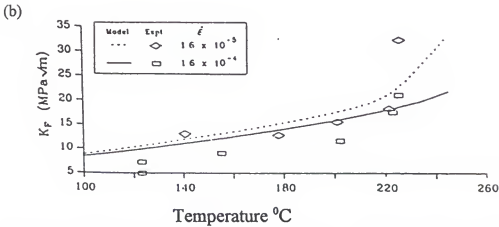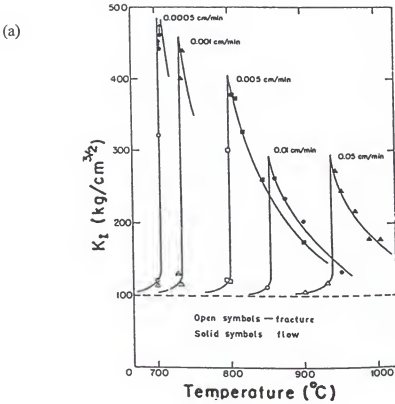
(a)

(b)

Figure 2.6 (a) Temperature vs. K_{IC} plot for Si single crystals at different strain rates showing a sharp BDT[58]. (b) Predicted and experimental BDT in Mo showing a gradual "soft" BDT[59].

to exhibit a gradual BDT [Figure 2.6 (b)][58-59]. In an experimental study on silicon single crystal, it was shown that the nature of the BDT can be changed from a "sharp" to "soft" by introducing more dislocations [Figure 2.7][61]. Similar results were shown by prestressing Ge single crystal[62]. Furthermore, it was shown that the BDTT of Si was decreased by introducing new dislocations by means of prestressing a crystal[60].

Several models have been proposed to explain the drastic increase in fracture toughness above the BDTT in various materials. According to a model proposed by Rice and Thomson[63], the BDT is associated with the spontaneous generation of dislocations. Hirsch and coworkers[58-60] proposed that the BDT is controlled by the motion of the preexisting dislocations to the crack tip which causes shielding of the crack tip. In this model, dislocations emitted from discrete sources along the crack front shield the crack tip. The condition for brittle fracture is that the local stress intensity factor K_e is equal to K_{IC} and the criterion for the BDT is that K_e is less than K_{IC} everywhere along the crack front for all values of the applied stress intensity factor K up to the value at which macroscopic yield takes place. It should be noted here that K_{IC} here refers to the low temperature fracture toughness in the brittle regime. In their early models, they used simple geometries of mode III (screw dislocations moving on a plane coplanar with a shear loaded crack) and mode I (edge dislocations moving on a plane normal to the crack). A schematic explaining these models is shown in Figure 2.8[59]. In their most recent model[58], they have simulated the motion of edge dislocations moving on a plane inclined at a general angle to the crack plane. The model functions by calculating the stresses on each dislocation in an array. In the earlier models, the source position was
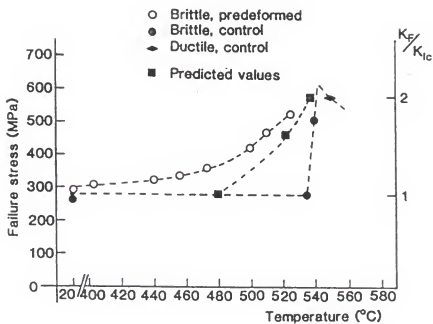
Figure 2.7 Effect of prestraining on Si single crystal on its BDT.[61]
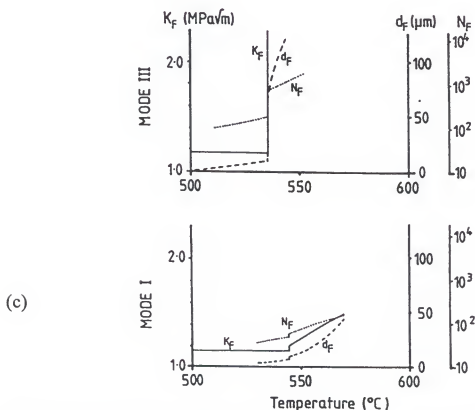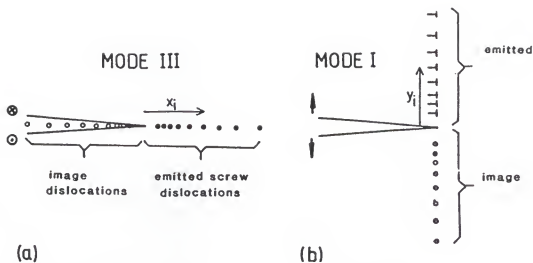
Figure 2.8 A schematic of Hirsch's model showing the geometry of (a) Mode III, and (b) Mode I simulations of dislocation arrays and cracks[59]. (c) Results of the Mode III and Mode I simulations of Hirsch's model[59].

chosen to be such that the first dislocation would be emitted at a stress intensity equal to that observed experimentally. In the recent model, they have used a source consisting of a dislocation dipole, the width and distance from the crack tip was chosen so that the dipole is separated, emitting a dislocation of one sign towards the crack at this value of applied K. The schematic of this model is shown in Figure 2.9. One limitation of this model is that it requires a realistic positioning of the dislocation source, which requires experimental data on the critical stress intensity required for the generation of the first dislocation in the material.

Ashby and Embury[64] proposed a simple model to show that when the lattice resistance limits the dislocation mobility, plasticity and blunting of the crack tip may be prevented simply because the nearest dislocations are too far away; the crack tip field is insufficient to move and multiply, dissipating energy and blunting the crack. At higher dislocation densities, dislocations lie closer to the crack tip; then the lattice resistance is exceeded by the crack tip field and dislocations move and multiply, dissipating energy and blunting the crack. This behavior is explained in Figure 2.10 (a). They also derived the dependence of the BDTT on dislocation density which suggests that the BDTT should decrease slowly as the dislocation density is increased up to a dislocation density of 10^{17} m/m^3. The model further predicts that the BDTT increases upon increasing the dislocation density beyond 10^{17} m/m^3. The results of their model are shown in Figure 2.10 (b).

Recently, a model combining the effects of dislocation mobility and generation was proposed[65]. Whether the BDT is controlled by the nucleation or by the motion of
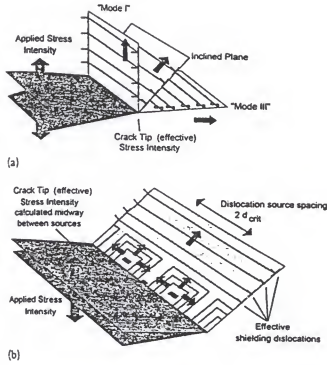
Figure 2.9 Roberts and Hirsch model simulating the motion of edge dislocations moving at a plane inclined at a general angle to the crack plane[58].
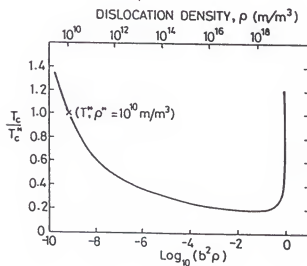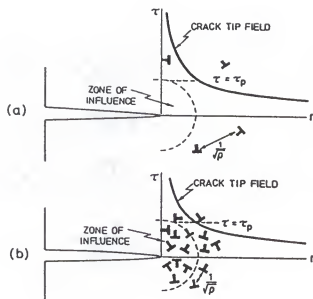
Figure 2.10 (a) and (b)Schematics of Ashby and Embury model[64]. (c) Results of Ashby model showing the variation of BDT with dislocation density[64].

dislocations, the initial dislocation density in the crack tip region seems to be an important factor in determining the BDTT of single crystals.

CHAPTER 3
MATERIALS AND EXPERIMENTAL PROCEDURES

The experimental approach taken in this study included conducting four-point bend and double-notched-tension tests for the evaluation of toughness and tensile tests for the evaluation of tensile properties, each of these under a set of thermal, mechanical, or physical conditions followed by fractographic analysis and slip trace analysis. The flow diagrams shown in Figures 3.1 and 3.2 show different steps schematically. These steps are described in detail in the following sections.

3.1 Single Crystal Procurement

Stoichiometric NiAl single crystals were procured from two different sources. The crystals used for the evaluation of toughness anisotropy and for studying the effects of notch type and heat treatment on toughness were procured from General Electric Corporation's Aircraft Division. The crystals used in the determination of the BDT, prestraining effects, displacement rate effects and tensile properties were grown at the University of Florida using a modified Bridgman technique.

```
┌─────────────────────────────────┐
│   Single crystal procurement    │
└─────────────────────────────────┘
              │
┌─────────────────────────────────┐
│      Homogenization at          │
│   1300°C for three hours +      │
│   cooled to RT at 2.4°C/min     │
└─────────────────────────────────┘
              │
┌─────────────────────────────────┐
│      Orienting the crystal      │
│       using Laue x-ray          │
│     backscattered technique     │
└─────────────────────────────────┘
              │
┌─────────────────────────────────┐
│  Specimen cutting using EDM     │
└─────────────────────────────────┘
              │
┌─────────────────────────────────┐
│   Electropolishing using 10%    │
│  perchloric acid +90% methanol  │
└─────────────────────────────────┘
              │
┌─────────────────────────────────┐
│      Prestraining under         │
│    tension at 200°C+            │
│         cooling                 │
│    under flowing argon          │
└─────────────────────────────────┘
              │
┌─────────────────────────────────┐
│   Introduction of notch         │
│   using a diamond blade         │
└─────────────────────────────────┘
              │
┌──────────────────┐  ┌───────────────┐
│ Fracture toughness│  │ Tensile testing│
│     testing      │  │   at various   │
│ at various temp.  │  │  temperatures  │
│ and strain rates │  │ and strain rates│
└──────────────────┘  └───────────────┘
```
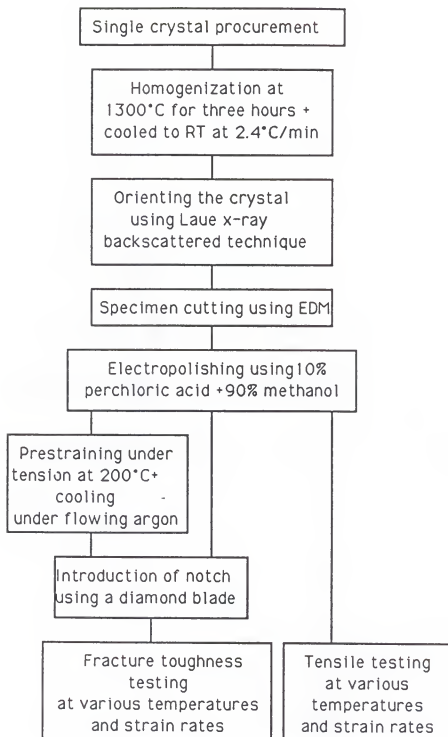
Figure 3.1 A flow diagram showing various steps in the preparation and testing of the double-notched-tension specimens.
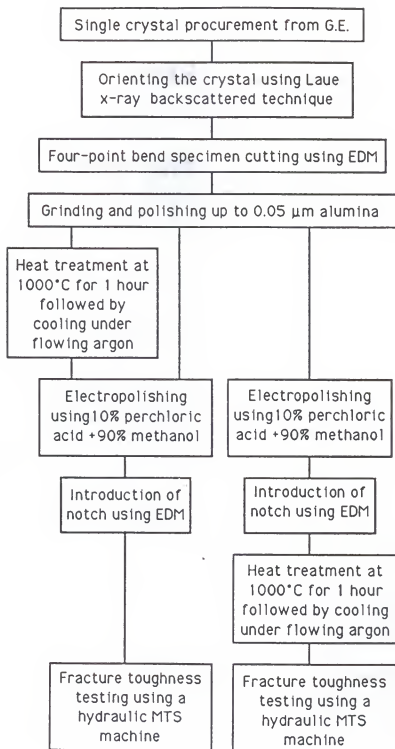
Figure 3.2 A flow diagram showing various steps in the preparation and testing of four point bend specimens.

3.2 Chemical Characterization of Single Crystals

The properties of NiAl single crystals are sensitive to the impurity concentration. The crystals used in the study were analyzed for their chemical composition. The compositional analysis of one crystal was performed at NASA-Lewis Center while the others were analyzed at the University of Florida using the Infra-red Coupled Plasma Emission (ICPE) Spectroscopy. The compositional analyses of different crystals are given in Table 3.1.

Table 3.1. Chemical composition of single crystals used in the study.

Crystal	wt %					
	Ni	Al	C	N	O	Si
A	68.47	31.36	—	—	—	0.17
B	68.31	31.60	—	—	—	0.09
C	68.67	31.28	—	—	—	0.05
D	68.26	31.66	—	—	—	0.08
E	68.67	31.32	0.0023	0.0003	0.0124	—

3.3 Homogenization Treatment

Considering the effects of point defects and vacancy concentration on mechanical properties, it was necessary to homogenize crystals and cool them at a controlled rate from the homogenizing temperature. The purpose of the homogenization treatment was two folds, viz., (i) to obtain a homogeneous distribution of substitutional impurities, and

(ii) to attain an equilibrium vacancy concentration at room temperature. The single crystals grown at the University of Florida (hereafter, termed as the UF crystals) were homogenized at 1300^0C for three hours and cooled at a rate of 0.04^0C/sec whereas the crystals grown at General Electric (hereafter, termed as the GE crystals) had been homogenized at 1316^0C for 50 hours and cooled under flowing argon. The homogenization treatment to the UF crystals was given in an Oxy-Gon furnace model FR200. The furnace was controlled by a microprocessor-based controller made by Honeywell, which was capable of controlling the heating and cooling rates with an accuracy of 0.002^0C/sec. Prior to homogenization, a 2 mm thick slice was cut off from the top of each crystal to remove the material of high impurity concentration. The homogenization treatment to the GE crystals was given at their works located in Evendale, Ohio. The UF crystals which were cooled slower are expected to have a lower concentration of thermal vacancies than the GE crystals.

3.4 Orientation Characterization

Homogenized single crystals were etched using aqua regia (2 parts by volume of HCl + 1 part by volume of HNO_3) by submerging the crystal in aqua regia solution and heating it for five minutes. The etching was done to remove the oxide layer from the crystal. In order for the aqua regia to be most effective in its action, it must be used nearly twenty four hours after it is prepared. Older solutions may take much longer in removing the layer and/or may require heating to higher temperatures.

Following the removal of the oxide layer, the crystals were analyzed for their orientation using Laue Back-scattered X-ray technique. The UF crystals were attempted to be grown such that <110> direction coincided with the longitudinal axis of the crystal. However, the crystals turned out to be nearly $6\text{-}8^0$ off from <110> direction. The crystals were oriented using a three-axis goniometer made by South Bay Technology, Inc. and Laue pictures were repeatedly taken until the crystals were oriented to accurately match the required specimen orientations. A similar procedure was used for orienting the GE crystals which were close to [100] direction along their longitudinal direction.

3.5 Specimen Cutting

The specimens were cut using an electric discharge machine (EDM). The appropriately oriented single crystals were transferred from the three-axis goniometer to the fixtures located on the electric discharge machine. Care was taken to avoid any changes in the orientations during this transfer. A traveling wire-EDM manufactured by Raycon/Brother model HS-100 was used in this study. The machine uses a 250 μm diameter consumable brass wire to discharge a spark between the wire and the crystal to be cut. The spark causes localized melting while the crystal moves through the wire. In this system, the crystal to be cut along with the mounting stage is movable and the movement can be programmed. Thus, the machine is capable of making very precise cuts including some of the relatively complex geometries such as arcs and circles. The sample holding stage and the wire are submerged in a dielectric fluid (de-ionized water) which also acts as a cooling medium.

3.5.1 Four Point Bend Specimens

Single-edge-notched four point bend (SENB) tests were used to characterize the toughness anisotropy and also to study the effects of heat treatments and the notch type on the fracture toughness. The specimens were rectangular bars of the size shown in Figure 3.3. Bend specimens of three different orientations were cut. These orientations were (101)[010], (101)[$\bar{1}$01], and (010)[100], respectively, where the plane indicates the notch plane and the direction indicates the direction of notch front. Four point bend fixtures with a lower span of 30 mm and an upper span of 20 mm were used in the testing. Therefore, the length of the specimens was chosen to be 35 mm. Using the ASTM standards[66], the width of 5 mm was chosen to comply with the requirement of $S_2=4W$. Similarly, the ratio of notch length to the width of the specimen was chosen to be 0.5.

3.5.2 Double-Notched-Tension Specimens

A double-notched-tension specimen geometry as shown in Figure 3.4 was adopted for determining the BDT and the effects of prestraining, heat treatments, strain rate and notch size. This geometry was primarily adopted because it allows a homogeneous prestraining to be performed prior to making notches. The specimen in the double-notched form were used for the determination of fracture toughness, whereas the specimens with same geometry, shape and size , but in "un-notched" form, were used for the characterization of tensile properties. The fixtures used in the study were made of
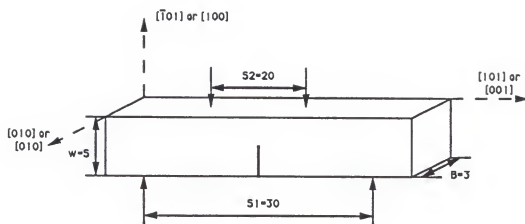
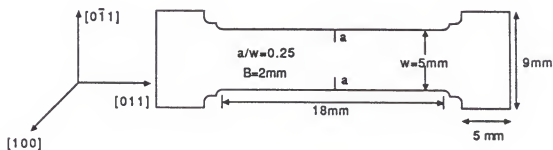Figure 3.3 A schematic showing the geometry and orientations of the four-point bend specimens.

Figure 3.4 A schematic showing the geometry and orientation of the double-notched tension specimens.

stainless steel and the head of the specimens was designed to fit in these fixtures. A double curvature as shown in Figure 3.4 was given to avoid sharp corners between the head and the guage. The guage length of these specimens was 18 mm. For the toughness testing, the ratio between the notch size and the width of the specimen was maintained to be 0.50. In order to maintain an accuracy in orientations, the following cutting scheme was used:

(i) The single crystals were mounted on the EDM machine such that the [100] direction was parallel to the wire and that the X and Y movement directions of the wire coincided with the [0$\bar{1}$1] and [011] directions of the crystal.

(ii) Slices of 2.5 mm thickness and having (011) as the largest face were cut without taking single crystal out of the machine. This ensured the similarity of orientation in all specimens and minimized deviations from the targeted orientations.

(iii) Slices were stacked horizontally using the appropriate fixtures and the specimens of the geometry shown in Figure 3.4 were cut using the cutting program entered in the machine.

3.6 Electropolishing

In order to remove the surface damage created during electric discharge machining, the specimens were electro-polished prior to toughness testing. The electropolishing was carried out using a DC power supply and a solution of 10% perchloric acid and 90% methanol. The specimens were submerged in the solution maintained at zero degree Celsius. A stainless steel cathode was used in the process. A

voltage controlled process was used wherein the current required to electropolish was calculated based upon the total surface area of the specimen. After conducting some preliminary trials, a current density of 0.60 A/cm^2 was found to give the best results. A lower current density causes etching while a higher current density causes pitting in the specimen. The tensile specimens were electro-polished for an eight minute period during which they were inverted after the first four minutes of polishing.

Bend specimens were mechanically polished using SiC paper and Al$_2$O$_3$ suspensions up to 0.5μm size prior to electropolishing. These specimens were electro-polished selectively near the center of the specimen using a selective removal process. In all cases, electropolishing was performed prior to making a notch.

3.7 Introduction of Notch

The notches were introduced using two different techniques (i) using the EDM, and (ii) using the low speed saw equipped with a diamond coated wafering blade. The notches created by the EDM had a notch root radius of 150 μm whereas the root radius of the notches created by the low speed saw varied depending on the thickness of the wafering blade. After a thorough investigation, the details of which are described in Appendix A, it was decided to use the low speed saw with a wafering blade of 300 μm thickness for making notches in this study. A low speed was used and no additional weight was used in the cutting process to minimize the stresses ahead of the notch. Blades of six inch diameter were used to maintain a linear notch front and the specimens were placed in the fixtures at such an angle that parallel notch fronts were obtained.

3.8 Prestraining

Selected specimens were prestrained in tension. The prestraining treatment was given at 200°C because NiAl single crystals did not show adequate ductility at temperatures below 200°C and the localized deformation (necking) began at low strain values at temperatures above 200°C. Prestraining was performed prior to introducing notches in a closed loop hydraulic MTS system. A strain rate of 5×10^{-4} sec^{-1} was used for prestraining. Four different levels of prestraining, viz., 1%, 5%, 10%, and 15% were used to study the effect of prestraining level on the room temperature fracture toughness. These four levels were chosen based upon the tensile stress-strain curve obtained at 200°C. A fixed prestrain level of 10% plastic strain was used for establishing the effect of prestraining on the BDT. The specimens were unloaded immediately after the prestrain level reached the desired value and the specimens were cooled to room temperature under flowing argon. One set of experiments was performed to vary the cooling conditions following the prestraining.

3.9 Heat Treatments

It was important to study the interactions of dislocations with various point-defects and their effects on toughness. Different dislocation/point-defect interactions were invoked by conducting different heat-treatments followed by toughness testing. Several sets of experiments were conducted to study the effect of heat treatment on the fracture toughness. In one set of experiments heat treatments were given at 500°C and

1200^0C and the specimens were cooled using water quenching, flowing argon through the furnace or by furnace cooling in a closed atmosphere. The heat treatments in different sets of experiments were conducted using ATS box furnaces, Oxy Gon furnace model FR200 or a CM mode 1600 vertical tube furnace. The Oxy Gon furnace was equipped with microprocessor based controllers which could control the heating and cooling rate with good accuracy.

3.10 Fracture Toughness Testing

Fracture toughness tests involving the heat-treatment effects were conducted using a screw driven Instron model 1125 at a displacement rate of 10^{-3} mm/sec. All other tests were conducted using a hydraulic closed-loop MTS machine. This machine was equipped with a furnace which can go up to 1600^0C. Chilled water was flown around the furnace chamber which kept the exterior of the furnace and the load cell cool. The furnace chamber is connected to a Balzers-Pfeiffer turbo pump which is capable of obtaining very high vacuums. The machine is connected to a HP plotter and also to a PC which records the data obtained by the machine using a "Labtech Notebook" software. The sensitivity of the HP plotter and the data acquired by the computer can be varied by altering the range over which the data is to be acquired. These ranges were varied in such a way that a maximum accuracy in the acquired data can be obtained.

The high temperature tests were conducted under flowing argon. The furnace chamber was evacuated to a vacuum level of 80 μm and back-filled with argon. This was repeated four times prior to heating the furnace to avoid the oxidation of the specimens

during the testing. Argon was continuously purified by passing it through a Ti containing gettering furnace prior to passing it through the furnace chamber. The specimens were slowly heated to the test temperature and soaked for one hour prior to testing. Allowing for sufficient soaking is very important especially at lower temperatures because of limited radiative or conductive heating in the given system. However, thermal equilibrium prevailed after a one hour soaking time. Tests were conducted at the desired displacement rates and the specimens were immediately cooled to room temperature under flowing argon upon completion of the tests.

Three displacement rates viz. 10^{-2}mm/sec, $2X10^{-4}$ mm/sec, and $2X10^{-5}$ mm/sec were used for establishing the BDT. Tests were conducted in the temperature range of room temperature to 400^0C with 50^0-100^0C intervals.

The fracture toughness of the four point bend specimens was calculated using the following formula[67]:

$$K_{Ic} = \frac{3P(s_1 - S_2)}{2BW^2} a^{1/2} Y(a/W) \qquad (3.1)$$

where B is the thickness, W is the width, a is the crack length, S_1 and S_2 are the loading spans, and Y (a/W) is the geometrical factor given by[68]:

$$Y(a/W) = 1.99 - 2.47(a/W) + 12.97(a/W)^2 - 23.17(a/W)^3 + 24.8(a/w)^4 \qquad (3.2)$$

The fracture toughness of the double-notched tensile specimens was calculated by[68]:

$$K_{IC} = Y\sigma\sqrt{a} \qquad (3.3)$$

where σ is the remote applied stress, a is the crack size and Y is a geometric factor which is given by[68]:

$$Y = 1.99 + 0.76(a/W) - 8.48(a/w)^2 + 27.36(a/W)^3 \qquad (3.4)$$

The crack size was taken to be equal to the notch size. Correcting for microcracks ahead of the notch did not make any significant difference in toughness values. At elevated temperatures, where the load-displacement curve was non-linear, the fracture toughness was calculated as K_{JC} using the following equation:

$$K_{JC} = K_Q + (J_p E)^{1/2} \qquad (3.5)$$

J_p was calculated from the area under the plastic regime of the load-displacement curves by using equation 3.6 and E is the modulus of elasticity. K_Q was calculated based upon the maximum load and using the equation 3.3[69].

$$J_p = \frac{2A}{bB} \qquad (3.6)$$

A is the area under the plastic regime of the load-displacement curve, b is the ligament size and B is the breadth of the specimen.

3.11 Tensile Testing

Tensile tests were conducted in the temperature range of room temperature to 300^0C at strain rates of 5×10^{-3} sec^{-1}, 5×10^{-5} sec^{-1}, and 5×10^{-6} sec^{-1}. Specimen geometry and orientations used for the tensile testing were the same as those used for the toughness testing. The only difference was that these specimens were not notched. The tests were conducted using the same closed loop hydraulic MTS machine as used for the toughness testing.

3.12 Microscopy

Fracture surfaces of the tested specimens were analyzed. Most of the analysis was done on a JEOL 200 SX scanning electron microscope (SEM) whereas JEOL 6400 SEM was employed in specific cases. In order to study the crack nucleation, a double-notched tension specimen was partially loaded at 350^0C and unloaded prior to its fracture. The specimen was analyzed for understanding the crack nucleation mechanism. Crack propagation paths were analyzed by observing crack profiles using the JEOL 200SX SEM and a Nikon PM-175A optical microscope.

The slip trace analysis on the prestrained specimens was performed using a Nikon PM-175A optical microscope. In order to unambiguously determine the slip plane, slip lines on two orthogonal planes were analyzed. A JEOL 200 SX scanning electron microscope was employed in some cases where the slip traces were deep and a higher depth of focus was required.

CHAPTER 4
RESULTS AND DISCUSSION

This chapter comprises of six sections. In the first section, results of tensile tests have been presented. The second section deals with the results of fracture toughness tests performed over a range of temperature and displacement rate. The third section includes prestraining procedure and effects of prestraining on room temperature toughness as well as on the BDTT. The toughness anisotropy and the effects of heat treatments on toughness have been presented in sections 4.4 and 4.5, respectively. The last section includes the results of fractography performed on the test specimens.

4.1 Tensile Properties

Tensile tests were performed at three different strain rates in the temperature range of room temperature to $300^{0}C$. The strain rates used were 5×10^{-3}, 5×10^{-5}, and 5×10^{-6} sec^{-1}. These tests were performed with the specimens of the same geometry and orientation as used for the toughness testing. Some tests were repeated to check the consistency of the data. The results were very consistent. The standard deviation for yield stress data was 2.7 MPa, for ductility 1.5%, and for fracture stress 14.7 MPa. The purpose of these tests was to obtain the tensile properties, viz., yield stress, ductility, strain hardening exponent, and fracture stress as a function of strain rate and temperature.

The yield strength and the strain hardening behavior obtained as a function of test temperature and applied strain rate was used for the analysis of the BDT as characterized by the toughness testing.

4.1.1 Stress-Strain Curves

Engineering stress-strain curves for the three strain rates are shown in Figure 4.1-4.3. Tensile properties for the three strain rates used are also listed in Tables 4.1-4.3. Figure 4.1 shows that specimens tested at very slow strain rates ($5x10^{-6}sec^{-1}$) at $20\,^0C$ and $100\,^0C$ fractured without any necking whereas the localized deformation started in specimens tested at 200^0C at nearly 4% strain. Following a small decrease in engineering stress up to a strain of 30%, the stress started to increase again and it continued to increase up to 56% strain. The specimen did not fracture and the test was stopped at this strain level.

Figure 4.2 shows the stress-strain curves for three temperatures at a strain rate of $5x10^{-5}$ sec^{-1}. Similar to the strain rate of $5x10^{-6}$ sec^{-1}, the specimens tested at 20^0C and 100^0C fractured without necking. At 200^0C, the localized deformation started at 10% strain. The stress decreased gradually up to about 30% strain and started to increase again. The specimen fractured at 61% strain.

Stress-strain curves for the strain rate of $5x10^{-3}$ sec^{-1} for different temperatures have been shown in Figure 4.3. The specimen tested at 200^0C fractured at 9.2% strain at this strain rate and necking did not precede fracture. The stress-strain curves obtained at 200^0C for the three different strain rates are compared in Figure 4.4. The comparison of
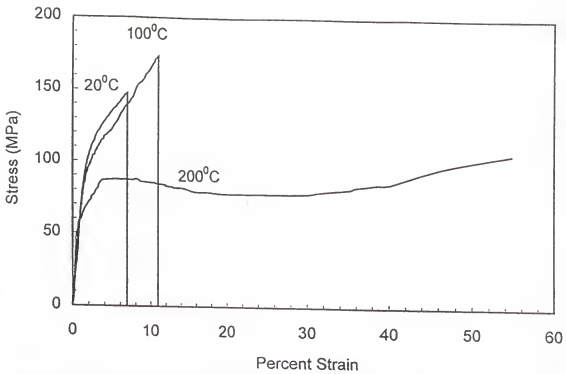
Figure 4.1 Engineering stress-strain curves obtained at various temperatures at a strain rate of 5X10⁻⁶ sec⁻¹.

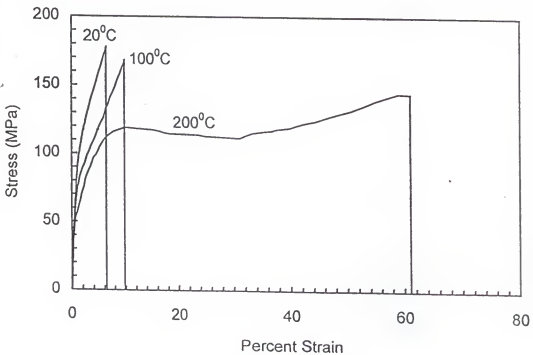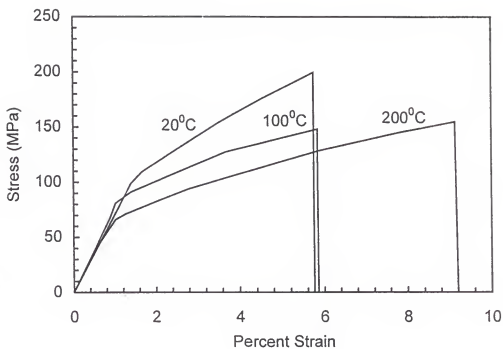Figure 4.2 Engineering stress-strain curves obtained at various temperatures at a strain rate of 5X10⁻⁵ sec⁻¹.

Figure 4.3 Engineering stress-strain curve obtained at various temperatures at a strain rate of 5×10^{-3} sec^{-1}.

the three curves shows a strong strain rate dependence of the strain hardening behavior, tensile ductility and maximum uniform strain. In general, the yield strength, the strain hardening rate and the maximum uniform strain decreased with an increase in test temperature and a decrease in applied strain rate. The strain rate and temperature dependence of various properties will be discussed in detail in the following sections.

Table 4.1. Tensile properties as a function of temperature at a strain rate of 5×10^{-3} sec^{-1}.

Temperature (°C)	Yield Stress (MPa)	True Fracture Stress (MPa)	Total Elongation (%)
20	109.7	211.3	5.8
100	83.4	150.9	5.8
200	69.2	168.1	9.1

Table 4.2. Tensile properties as a function of temperature at a strain rate of 5×10^{-5} sec^{-1}.

Temperature (°C)	Yield Stress (MPa)	True Fracture Stress (MPa)	Total Elongation (%)
20	98.0	189.4	6.3
100	75.5	185.6	10
200	55.7	-	61
300	28.1	-	>63.5

Table 4.3. Tensile properties as a function of temperature at a strain rate of 5×10^{-6} sec^{-1}.

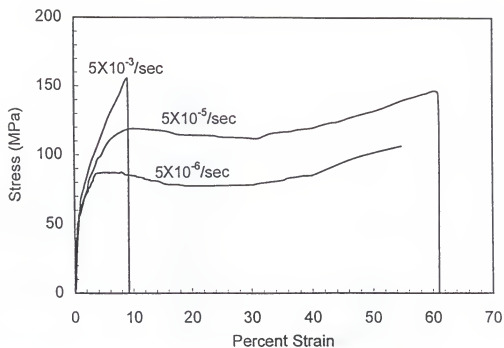| Temperature (°C)	Yield Stress (MPa)	True Fracture Stress (MPa)	Total Elongation (%)
20	94.8	163.5	6.9
100	83.8	191.9	11.0
200	55.7	-	>55.9

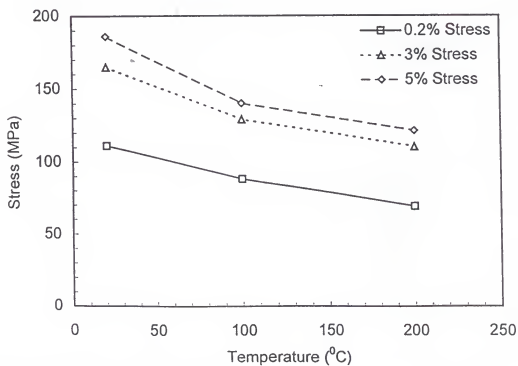Figure 4.4 Effect of strain rate on the tensile behavior at 200°C.

Figure 4.5 Effect of temperature on the flow stress at a strain rate of 5×10^{-3} sec^{-1}.

4.1.2 Temperature and Strain Rate Dependence of Flow Stress

Flow stress values at 0.2%, 3%, and 5% plastic strains were determined from the stress-strain curves at all temperatures and strain rates used in the study. These stress values are plotted as a function of temperature in Figures 4.5-4.7. $\sigma_{0.2\%}$ values for various test temperatures and strain rates are also given in Table 4.4. The standard deviation of yield stress data was 2.7 MPa. Figure 4.5 shows the temperature dependence of the flow stress at a strain rate of 5×10^{-3} sec^{-1}. It shows that flow stress at different strain levels, viz., $\sigma_{0.2\%}$, $\sigma_{3\%}$, and $\sigma_{5\%}$ decreases with an increase in temperature. This behavior is similar to the BCC metals which show a strong temperature dependence of the yield strength. This figure also shows that $\sigma_{5\%}$ shows a stronger temperature dependence than $\sigma_{0.2\%}$. This behavior reflects the temperature dependence of strain hardening behavior.

Table 4.4. Temperature and strain rate dependence of the 0.2% yield stress.

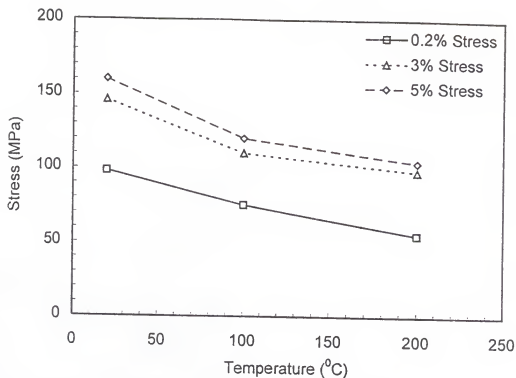| Temperature	Yield Stress (MPa)		
(^{0}C)	5×10^{-3} sec^{-1}	5×10^{-5} sec^{-1}	5×10^{-6} sec^{-1}
20	109.7	98.0	94.8
100	83.4	75.5	83.8
200	69.2	55.7	55.7
300		28.1	

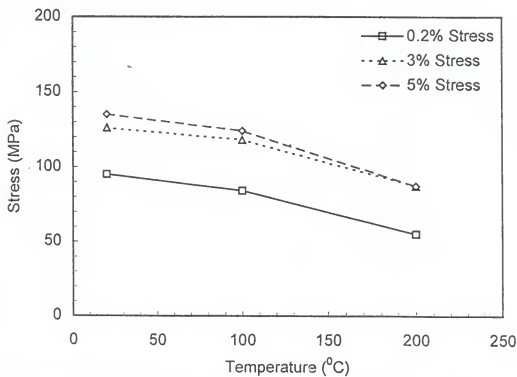Figure 4.6 Effect of temperature on the flow stress at a strain rate of 5×10^{-5} sec^{-1}.

Figure 4.7 Effect of temperature on the flow stress at a strain rate of 5×10^{-6} sec^{-1}.

Figure 4.6 shows the temperature dependence of flow stress at a strain rate of 5×10^{-5} sec^{-1}. It shows a behavior similar to that at the strain rate of 5×10^{-3} sec^{-1}. However, when the strain rate is very slow, the behavior is somewhat different. The temperature dependence of flow stress at a strain rate of 5×10^{-6} sec^{-1} is shown in Figure 4.7. At this strain rate, the rate of decrease in flow stress increases with temperature (the curve is concave downward) contrary to the results at higher strain rates which showed the conventional behavior, i.e., the decrease in flow stress becomes less significant at higher temperatures. This behavior is most likely due to the strain aging that may have occurred at 100°C in the slow strain rate tests. Strain aging has been reported to occur in NiAl previously by Weaver and Kaufman[45] and Hack et al[9]. Strain aging can cause the flow stress to increase anomalously within a specific temperature and strain rate range. The present investigation shows that NiAl single crystals of the <110> tensile orientation are particularly susceptible to strain aging at a strain rate of 5×10^{-6} sec^{-1} and temperature of 100°C. The other noticeable difference in this curve is that $\sigma_{3\%}$ and $\sigma_{5\%}$ have nearly the same values at this strain rate. This is due to the fact that necking started at low strain levels at this strain rate.

The temperature dependence of $\sigma_{0.2\%}$ has been compared for different strain rates in Figure 4.8. This figure illustrates the anomalous behavior at the slowest strain rate used where the yield stress increases with a decrease in applied strain rate. A similar comparison for $\sigma_{5\%}$ is made in Figure 4.9.

In order to determine the strain rate sensitivity, the logarithmic of the 0.2% flow stress was plotted as a function of the logarithmic of strain rate is shown in Figure 4.10
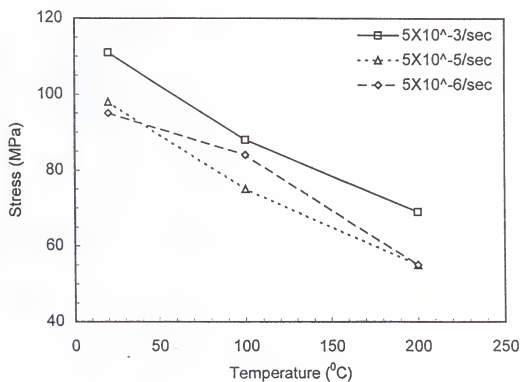
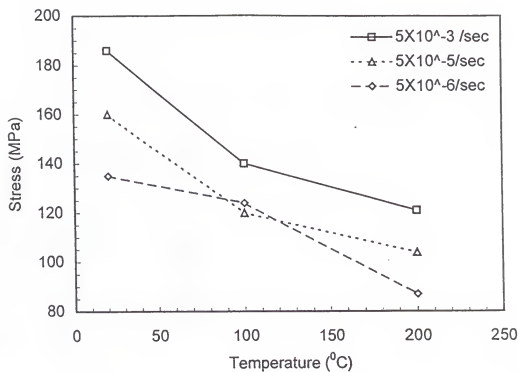Figure 4.8 A comparison of the temperature dependence of 0.2% flow stress at different strain rates.

Figure 4.9 A comparison of the temperature dependence of 5% flow stress at different strain rates.
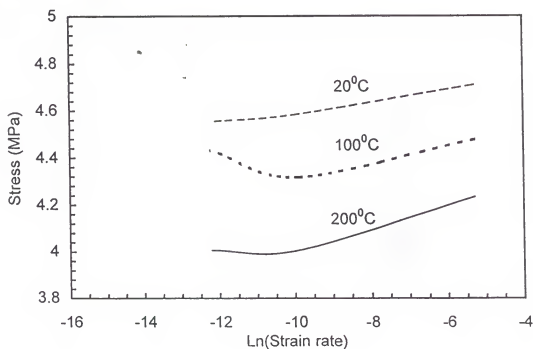

Figure 4.10 Logarithmic of 0.2% flow stress vs. Logarithmic of strain rate.

for the three test temperatures. This figure shows that for the 20^{0}C test temperature, the curve is almost linear, whereas for the other two test temperatures, the curves show two different slopes. Strain rate sensitivity "m" values were determined from each segment of the slope independently and the values are given in Table 4.5. It must be noted here that a negative m value indicates strain aging. Therefore, the m values obtained from the two higher strain rates were used to analyze the strain rate sensitivity of NiAl single crystals. The m values varied in the range of 0.02-0.05 in the temperature range used in this study. These are relatively low strain rate sensitivity values. Strain rate sensitivity did not vary with temperature between 20^{0}C and 100^{0}C where a constant m value of 0.02 was obtained for both the temperatures. At 200^{0}C, strain rate sensitivity increased to 0.05. These strain rate sensitivity values are in excellent agreement with the previously reported values by Takasugi et al[30].

Table 4.5: Strain rate sensitivity as a function of temperature

Temperature (^{0}C)	Strain Rate Sensitivity (m)	
	High strain rates	Low Strain rates
20	0.02	0.01
100	0.02	-0.5
200	0.05	

4.1.3 Temperature and Strain Rate Dependence of Strain Hardening Exponent

Strain hardening exponent "n" was determined for different strain rates and temperatures by plotting logarithmic of stress against the logarithmic of strain in the region of uniform plastic strain. These curves have been plotted in Appendix B in Figures B1-B9. As described in the Appendix, the curves fitted reasonably well using a linear regression which follows the Holloman relationship. Strain hardening exponent n was determined from the slopes of each of these curves. The n values for different temperatures and strain rates are given in Table 4.6. The standard deviation for n values was 0.02.

Table 4.6: Strain hardening exponent as a function of temperature and strain rate.

Temperature (°C)	Strain Hardening Exponent (n)		
	5×10^{-3} sec^{-1}	5×10^{-5} sec^{-1}	5×10^{-6} sec^{-1}
20	0.52	0.36	0.28
100	0.36	0.35	0.35
200	0.40	0.32	0.25

The strain hardening exponent is plotted as a function of strain rate for the three test temperatures in Figure 4.11. As seen from this figure, the strain hardening exponent is strongly dependent on the strain rate for the test temperatures of 20^0C and 200^0C. At these temperatures, the strain hardening exponent increases with increasing strain rate. This behavior is contrary to the behavior of BCC metals where strain hardening rate does

not vary significantly with strain rate. In this regard, NiAl seems to be behaving similar to the FCC and HCP metals where cross-slip of dislocations and hence the strain hardening varies with strain rate and temperature. On the other hand, at 100^0C, the strain hardening exponent did not vary with the strain rate. This anomalous behavior at 100^0C seems to be a result of the strain aging phenomenon occurring at this temperature.

The other interesting observation from Figure 4.11 is that the difference between the strain hardening exponents at 20^0C and 200^0C is much larger at the high strain rate ($5x10^{-3}$ sec^{-1}) as compared to that at the slow strain rate ($5x10^{-5}$ sec^{-1}). This can also be interpreted as the rate of change of strain hardening exponent with strain rate is larger at 20^0C as compared to that at 200^0C. This behavior may be reminiscent of the Arrhenius relationship between the temperature and the strain rate. The slope of the strain hardening exponent versus strain rate curve may, thus, exhibit an Arrhenius relationship with temperature.

Strain hardening exponent has been plotted as a function of temperature in Figure 4.12. In general, the strain hardening exponent decreases from 20^0C test temperature to 200^0C test temperature except for the data at 100^0C, where strain aging is prevalent. The increase in strain hardening exponent at low temperatures seems to be most significant at the highest applied strain rates. At the slowest strain rate, the strain hardening exponent slightly decreases from 20^0C to 200^0C. At this strain rate, the strain hardening exponent is anomalously high at 100^0C due to strain aging.
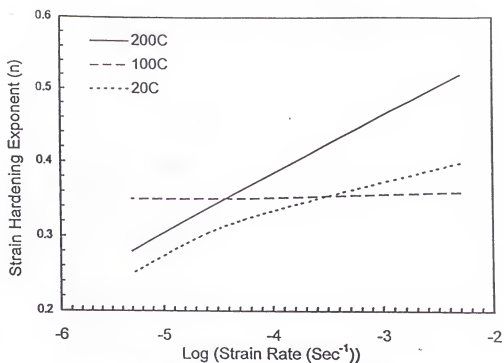
Figure 4.11 Effect of strain rate on the strain hardening exponent at various test temperatures.
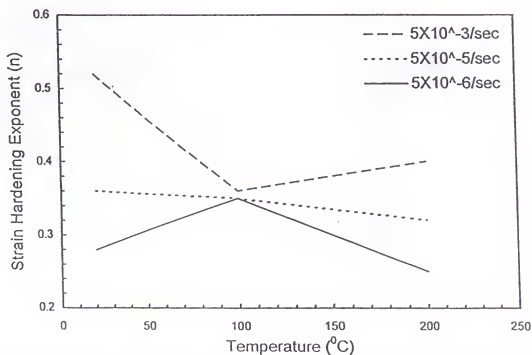

Figure 4.12 Effect of test temperature on the strain hardening exponents at different strain rates.

4.1.4 Tensile Ductility and Fracture Stress

Tensile elongations obtained at different test temperatures and strain rates are given in Tables 4.1-4.3. The data show that at 20^0C, nearly 6% tensile ductility was obtained. The ductility did not vary significantly with strain rate at 20^0C whereas at 200^0C, the ductility was strongly dependent on strain rate. At 200^0C, the ductility was 9% for the strain rate of $5x10^{-3} sec^{-1}$ which increased to 61% for a strain rate of $5x10^{-3} sec^{-1}$. Upon further decreasing the strain rate, excessively high elongations were obtained and the test was stopped due to unusually long testing time involved. At 100^0C test temperature, the ductility increased from 5.8% at a strain rate of $5x10^{-3} sec^{-1}$ to 10% and 11% at $5x10^{-5} sec^{-1}$ and $5x10^{-6} sec^{-1}$, respectively.

For a given strain rate, ductility increased with increasing temperature and the extent of increase was higher for slower strain rates. At a strain rate of $5x10^{-3} sec^{-1}$, the ductility increased from 5.8% at 20^0C to 9.1% at 200^0C whereas for a strain rate of $5x10^{-5} sec^{-1}$, the ductility increased from 6.3% to 61% over the same temperature range.

True fracture stress values at different temperatures and strain rates are given in Tables 4.1-4.3. True fracture stress values were calculated for specimens which failed within the uniform deformation regime. For a strain rate of $5x10^{-5} sec^{-1}$, the fracture stress was independent of temperature. The fracture stress is considered to be independent of temperature and strain rate, however, variations in the initial surface condition may cause scatter in the data.

4.1.5 Calculation of Activation Energy

Activation energy associated with the thermally-activated deformation of NiAl single crystals was determined. A power law approach suggested by Reed-Hill et al[70-72] was used for estimating the activation energy and activation volume. The basic assumption in the model is that the effective stress, in the absence of strain aging, obeys the power law given by the following equation

$$\sigma^* = \sigma_0^* \left(\frac{\dot{\epsilon}}{\dot{\epsilon}_0} \right)^{\frac{RT}{H^0}} \qquad (4.1)$$

where σ^* is the effective stress, σ_0^* is the effective stress at 0K, $\dot{\epsilon}$ is the applied strain rate, ϵ_0 is a material constant equivalent to the strain rate that makes $\sigma^* = \sigma_0^*$ at any temperature, R is the gas constant, T is the absolute temperature, and H^0 is a material constant indicating the stress dependence of activation enthalpy.

Using the above model, the logarithmic of $\sigma_{0.2\%}$ was plotted as a function of temperature for two strain rates. The lowest strain rate could not be used in this calculation due to the occurrence of strain aging. The data fitted very well into linear curves as shown in Figure 4.13. The intercepts of these curves were obtained. The average of the exponentials of these intercepts gives σ_0^*. In the second step, the negative values of the slopes of the curves in Figure 4.13 were plotted as a function of logarithmic of strain rate. From the Power Law, the slope of this curve is equal to R/H^0. Thus, H^0 values were obtained. Similarly, ϵ_0 was obtained from the slope and intercept of this
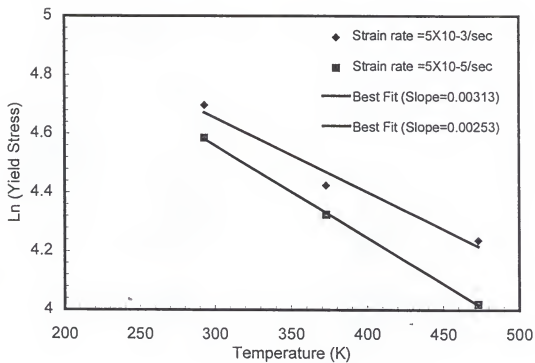
Figure 4.13 Logarithmic of yield stress as a function of temperature.

curve and by using the power law in the forms of equations (4.2) and (4.3). By rewriting equation (4.1):

$$\ln\left(\frac{\sigma^*}{\sigma_0^*}\right) = \frac{RT}{H^0}\ln(\varepsilon^\cdot) - \frac{RT}{H^0}\ln(\varepsilon_0^\cdot) \tag{4.2}$$

By differentiating the above equation we obtain,

$$\frac{\partial\ln\left(\frac{\sigma^*}{\sigma_0^*}\right)}{\partial T} = \frac{R}{H^0}\ln(\varepsilon^\cdot) - \frac{R}{H^0}\ln(\varepsilon_0^\cdot) \tag{4.3}$$

The calculated values of the power law parameters for NiAl single crystals are given in Table 4.9.

Activation volume (v^*) was calculated using the following equation:

$$v^* = \frac{H^0}{\sigma^*} = \frac{H^0}{\sigma_0^* e^{-\beta T}} \tag{4.4}$$

where β is the slope of the curves shown in Figure 4.13. Using the above parameters, the

Table 4.9: Calculated values of the Power Law parameters for NiAl single crystals.

Parameter	Value
σ_0^*	234.4 MPa
H^0	63.4 KJ/mole
ϵ_0	1.2×10^6 sec^{-1}

activation energy was calculated at different applied stress levels using the following equation:

$$H = H^0 \ln \left(\frac{\sigma^*}{\sigma_0^*} \right) \qquad (4.5)$$

The calculated values of the activation energy and activation volumes have been plotted as a function of stress level in Figure 4.14 and 4.15. These figures show that there is a strong stress dependence to the activation energy associated with the thermally assisted deformation of NiAl single crystals. From these calculations, activation volume at the stress values normally encountered in the deformation of NiAl seems to be equivalent to a cube of three times the Burgers vector of NiAl.

4.2 Brittle-to-ductile transition

Brittle-to-ductile transition of NiAl single crystals was established by conducting fracture toughness tests at various temperatures using the double-notched tension specimens. The BDT curve evaluated in the form of J_{IC} for a displacement rate of 10^{-2} mm/sec is plotted in Figure 4.16. The change of toughness with temperature at low temperatures can be demonstrated clearly when the toughness is plotted in the form of K_{JC} as shown in Figure 4.17. The procedures for calculating K_{JC} and J_{IC} have been described in detail in section 3.10. The curves show the presence of three distinct regions as marked in Figures 4.16 and 4.17. In region I fracture occurred within the linear portion of load-displacement curve. The transition between region I and region II
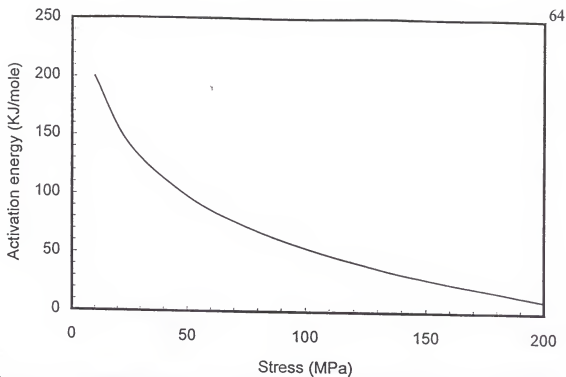
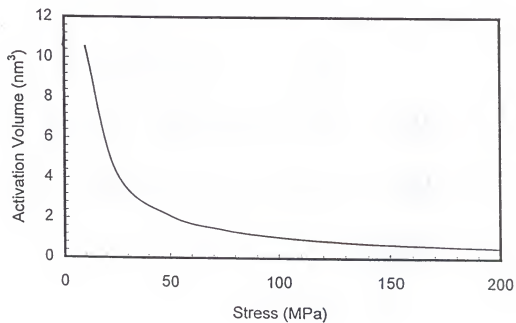Figure 4.14 Activation energy vs. Applied stress predicted based upon Reed-Hill model.

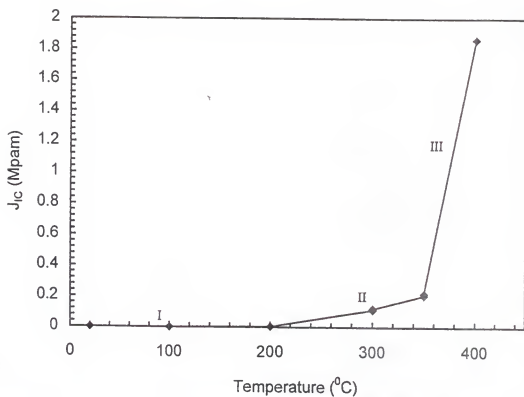Figure 4.15 Activation volume vs. applied stress predicted based upon Reed-Hill model.

Figure 4.16 J_{IC} as a function of temperature for a displacement rate of 10^{-2} mm/sec.
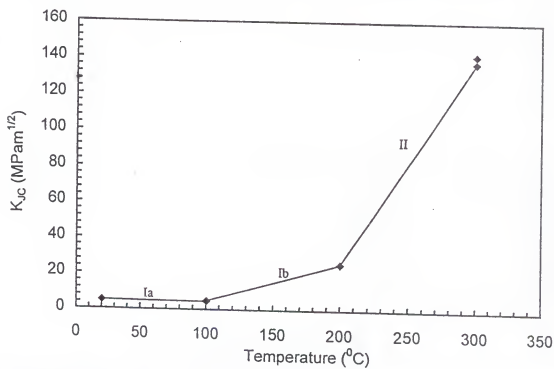

Figure 4.17 K_{JC} as a function of temperature for a displacement rate of 10^{-2} mm/sec.

occurred when the net-section yielding took place. The net-section yielding was manifested as non-linearity in the load-displacement curve. In other words, if the fracture occurs in the linear regime, the load-displacement curves show a sudden load-drop to zero following the linear portion of the curve whereas if the net-section yielding precedes the fracture, the load-displacement curve changes from linear to non-linear prior to the unstable fracture. This is shown clearly in Figure 4.18 which contains the load-displacement curves of the specimens tested at different temperatures at a loading rate of 10^{-2} mm/sec. Figure 4.18 reveals that the specimens tested at room temperature and 100^0C fractured within the linear portion of load-displacement curve whereas the specimens tested at 200^0C and 300^0C showed a non-linear portion of the load-displacement curve prior to their fracture indicating that the specimens at 200^0C and 300^0C had undergone the net-section yielding prior to their fracture.

The regime I, as shown in Figure 4.17, represents the linear-elastic (Ia) and elastic-plastic (Ib) deformation modes. In the linear elastic regime, the plastic zone that develops at the crack tip is much smaller than the specimen dimensions (small scale yielding). An elastic-plastic fracture mode implies that the plastic zone size is large, however, the plastic zone size is smaller than the ligament (the distance between the two notches) of the specimen. At the net-section yielding, the plastic zones at the two notches join and the entire cross-section within the notches deforms plastically.

The transition between region II and region III is associated with the general yielding where the whole specimen deforms plastically. A specimen fractured in region III shows extensive plasticity.
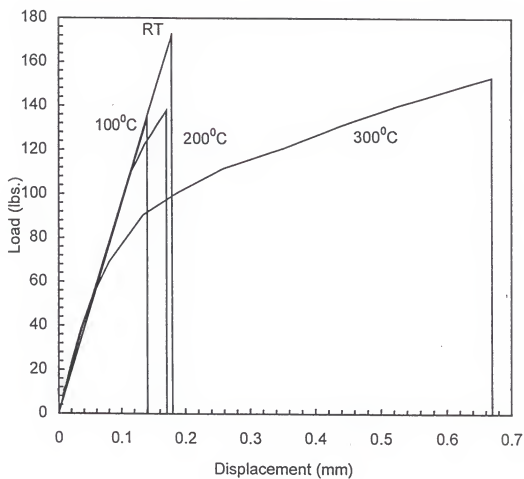
Figure 4.18 Load-displacement curves for toughness tests at different temperatures at a displacement rate of 10^{-2} mm/sec.

The BDTT is defined as the temperature at which the toughness starts to increase drastically. Figure 4.17 shows that in the case of NiAl single crystals, it coincides with the temperature at which the net-section yielding takes place. It should be noted here that the occurrence of the net-section yielding is dependent on the specimen size. If the specimen size was larger than the size used in this study, the net-section yielding may not have occurred, however, the specimen would have undergone the BDT. In that case, the BDT would be more gradual and the BDT temperature would be associated with a change in deformation mode from small scale yielding to large scale yielding. As seen from Figure 4.17, the BDT had taken place at 200^0C at the displacement rate of 10^{-2} mm/sec. However, since the toughness measurements were carried out at finite temperature intervals, the BDTT is being calculated as the average of the lowest test temperature which showed the net-section yielding and the highest test temperature which did not show the net-section yielding. Thus, the BDTT at the displacement rate of 10^{-2} mm/sec is 150^0C.

4.2.1 Effect of Displacement Rate

The BDT curves were established for three displacement rates, viz., 10^{-2} mm/sec, $2X10^{-4}$ mm/sec, and $2X10^{-5}$ mm/sec. The fracture toughness in the form of J_{IC} and K_{JC} are plotted as a function of temperature for the three displacement rates used in the study in Figures 4.19 and 4.20, respectively. The toughness values at different temperatures in the form of J_{IC} and K_{JC} are also given in Tables 4.10 and 4.11, respectively. These data show that the BDTT of NiAl single crystals is strongly dependent on the displacement
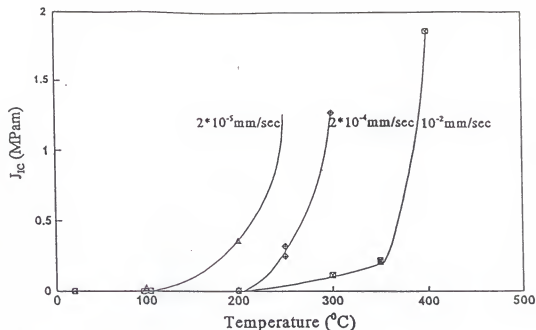
Figure 4.19 Fracture toughness (J_{Ic}) as a function of temperature for three applied displacement rates.
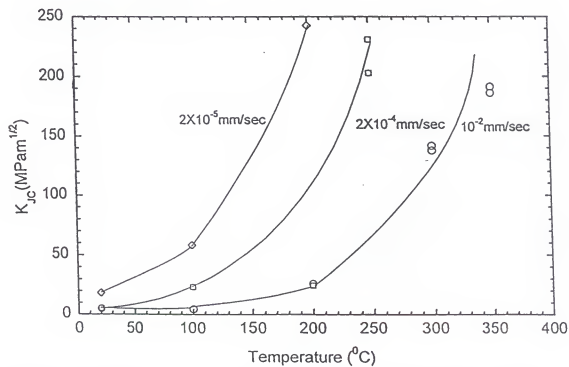

Figure 4.20 Fracture toughness (K_{Ic}) as a function of temperature for three applied displacement rates.

rate. As seen from these data, the BDTT decreases with decreasing displacement rates. It should be noted here that the toughness values change with a change in displacement rate when there is a change in the load-displacement behavior, e.g., the toughness values of specimens tested at room temperature at 10^{-2} mm/sec and 2×10^{-4} mm/sec are similar because both of these specimens fail in a linear-elastic regime whereas the specimen tested at room temperature at 2×10^{-5} mm/sec showed a high toughness because it had undergone the net-section yielding at room temperature.

Table 4.10: Effect of displacement rate on the BDTT as evaluated by J_{IC}.

Tempera ture (°C)	Displacement Rate					
	10^{-2} mm/sec		2×10^{-4} mm/sec		2×10^{-5} mm/sec	
	J_{IC} (KPam)	Load-displaceme nt behavior	J_{IC} (KPam)	Load-displaceme nt behavior	J_{IC} (KPam)	Load-displaceme nt behavior
20	0.123	Linear	0.144	Linear	1.99	Non-linear
100	0.103	Linear	3.27	Non-linear	20.2	Non-linear
100	0.121	Linear				
200	3.99	Non-linear	3.51	Non-linear	349	Non-linear
250			245	Non-linear	>>566	Crack did not go unstable
250			317	Non-linear		
300	113	Non-linear	1270	Non-linear		
300	120	Non-linear				
350	206	Non-linear				
350	218	Non-linear				
400	1864	Non-linear				

Table 4.11. Effect of displacement rate on the BDTT as evaluated by K_{JC}.

Temperature (°C)	Displacement Rate					
	10^{-2} mm/sec		2×10^{-4} mm/sec		2×10^{-5} mm/sec	
	K_{JC} (MPam$^{1/2}$)	Load-displacement behavior	K_{JC} (MPam$^{1/2}$)	Load-displacement behavior	K_{JC} (MPam$^{1/2}$)	Load-displacement behavior
20	5.0	Linear	5.4	Linear	18.3	Non-linear
100	4.6	Linear	24.3	Non-linear	58.2	Non-linear
100	5.0	Linear				
200	25.9	Non-linear	24.3	Non-linear	242.3	Non-linear
250			203.0	Non-linear	>>308.0	Crack did not go unstable
250			230.9	Non-linear		
300	138.1	Non-linear	461.8	Non-linear		
300	142.0	Non-linear				
350	186.2	Non-linear				
350	191.6	Non-linear				
400	559.4	Non-linear				

The load-displacement curves for the other two displacement rates used in this study are shown in Figures 4.21-4.22. Figure 4.21 shows the load-displacement curves obtained for a loading rate of 2×10^{-4} mm/sec. These curves show that at room temperature the fracture occurred within the linear-elastic portion of the load-displacement curve for this displacement rate. However, the test at 100°C showed the net-section yielding prior to the unstable fracture of the specimen. In other words, the
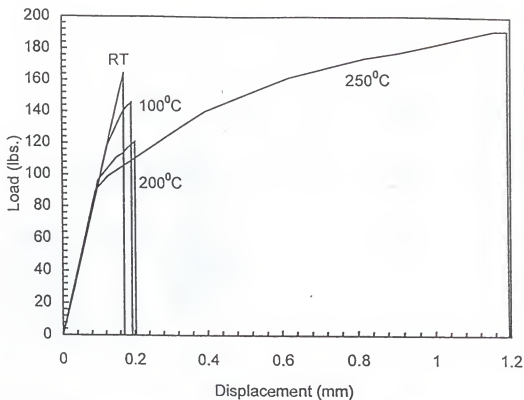
Figure 4.21 Load-displacement curves for toughness tests at different temperatures at a displacement rate of 2X10⁻⁴ mm/sec.
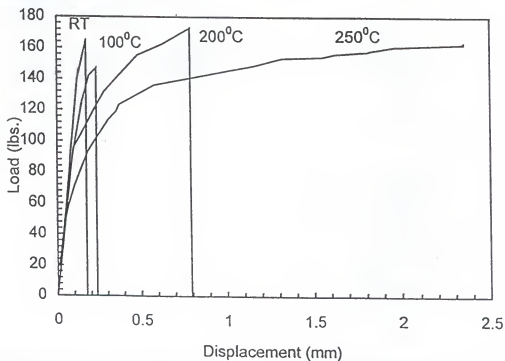

Figure 4.22 Load-displacement curves for toughness tests at different temperatures at a displacement rate of 2X10⁻⁵ mm/sec.

BDT had taken place at 100^{0}C for the displacement rate of 2×10^{-4} mm/sec. The load-displacement curves for the displacement rate of 2×10^{-5} mm/sec are shown in Figure 4.22. As seen from these curves, the net-section yielding occurred at room temperature at this displacement rate. In other words, the BDT had taken place at room temperature for a displacement rate of 2×10^{-5} mm/sec.

The load-displacement curves for three displacement rates have been compared in Figures 4.23-4.25. A comparison of the load-displacement curves at 100^{0}C [Figure 4.23] shows that the fracture occurred within the linear-elastic portion of the load-displacement curve for the highest displacement rate at 100^{0}C whereas the two lower displacement rates exhibited the net-section yielding prior to the unstable fracture at this test temperature. A comparison of the load-displacement curves at 200^{0}C [Figure 4.24] shows that the net-section yielding had occurred at all three displacement rates at this temperature and an extensive deformation was obtained for the displacement rate of 2×10^{-5} mm/sec. The load-displacement curves at 300^{0}C have been compared in Figure 4.25. These curves show that the specimen tested at 2×10^{-4} mm/sec showed an extensive deformation at this temperature. It is obvious from these load-displacement curves that the displacement rate and temperature both affect the commencement of the net-section yielding as well as the resistance to further plastic deformation as manifested by the rate of increase in load with displacement (equivalent to the strain hardening rate). It was described in section 4.1 that the yield strength and the strain hardening rate both vary with temperature and strain rate in NiAl single crystals. Stress distribution ahead of the notch in toughness tests depends on the yield strength. Since the yield strength changes
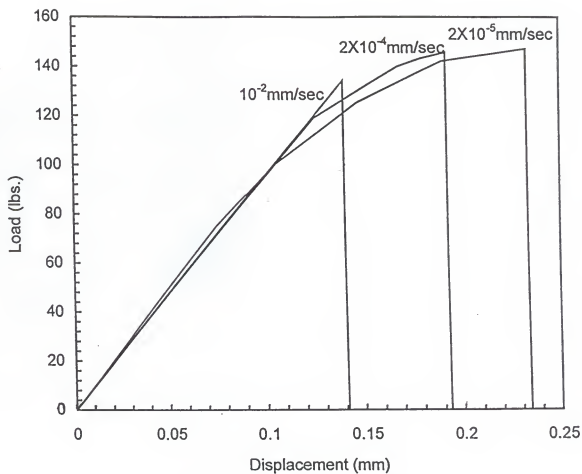
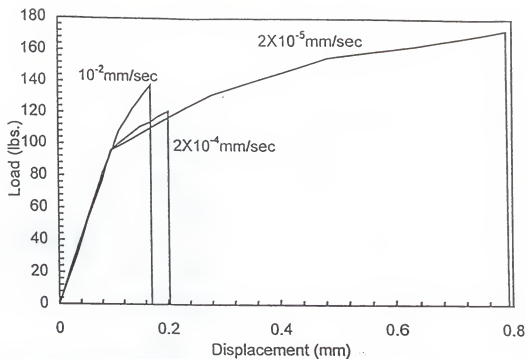Figure 4.23 Load-displacement curves for toughness tests at different displacement rates 100°C.

Figure 4.24 Load-displacement curves for toughness tests at different displacement rates at 200°C.
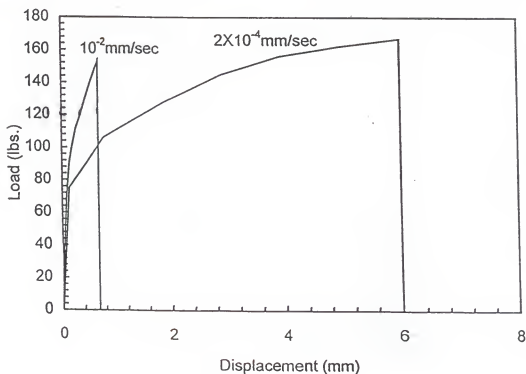

Figure 4.25 Load-displacement curves for toughness tests at different displacement rates at 300°C.

with temperature and strain rate, it alters the stress distribution ahead of the notch tip, which defines the plastic zone size. The net-section yielding starts when the plastic zone size becomes equivalent to the size of the ligament. Therefore, the strain rate and the temperature govern the commencement of the net-section yielding. The change in strain hardening behavior also alters the stress distribution ahead of the notch, so, it enhances the observed effects of displacement rate and temperature on the commencement of the net-section yielding. Thus, the displacement rate dependence of the BDTT is a result of the strain rate dependence of the yield strength and the strain hardening rate.

4.2.2 Determination of Activation Energy

The activation energy associated with the BDT has been estimated by using the Arrhenius relationship between the BDT temperature and the applied loading rate. The logarithmic of the applied loading rate has been plotted as function of the observed BDTT in Figure 4.26. The activation energies have been calculated from the slopes of these curves and have been given in Table 4.12. As the table shows, the activation energy associated with the BDT has been estimated to be 48.4 KJ/mole. The activation energy for diffusion of Ni in NiAl single crystals has been reported to be about 197 KJ/mole[73,74]. The activation energy associated with the BDT compares well with the estimated activation energy for thermally assisted deformation of NiAl single crystals based upon the Reed-Hill model [see Figure 4.14]. The calculations performed based on this model indicate that the activation energy of the thermally assisted deformation of NiAl single crystals is dependent on the applied stress level. From Figure 4.14, the activation energy
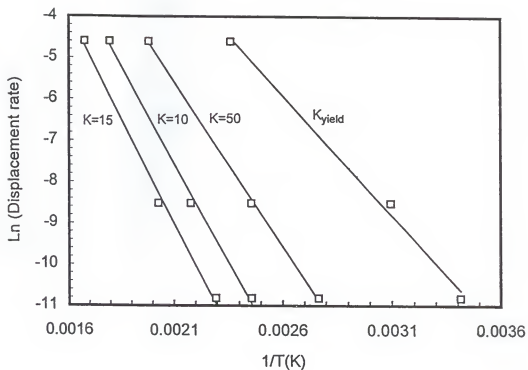
Figure 4.26 Logarithmic of displacement rate as a function of temperature for different stress intensity (K) levels.

under an applied stress of 100 MPa is 50 KJ/mole and under an applied stress of 50 MPa

it is about 100 KJ/mole. The activation energy values shown in Table 4.12 are within this

range indicating that they were evaluated under an applied stress level of 50-100 MPa.

These data indicate that thermally assisted deformation is responsible for the occurrence

of the BDT in NiAl single crystals. The activation energies were also calculated at

several stress intensity (K) levels. Activation energies corresponding to higher K levels

are higher than the activation energies at the BDTT. It should be noted here that a higher

K level here does not imply a higher applied stress level. Higher K level, on the other

hand, indicates that measurements were done at higher temperatures which reflect

relatively low stress levels.

Table 4.12: Activation energies and slopes at different K levels.

K Level (MPam$^{1/2}$)	Slope	Activation Energy (KJ/mole)
Net-Section Yielding	-5823.4	48.4
50	-7973.0	66.3
100	-9488.7	78.9
150	-10148.9	84.4

4.3 Effect of Prestraining on Toughness

4.3.1 Prestraining Procedure

The tensile data revealed that below 200^{0}C the specimens failed with very low

ductility and above 200^{0}C the localized deformation (necking) started at relatively low

strain values. Therefore, 200°C was found to be an optimum temperature for prestraining. The engineering stress-strain curve at 200°C is shown in Figure 4.27. The curve shows the four prestrain levels chosen for toughness measurements. The yield stress of this crystal was 69 MPa at 200°C and the maximum uniform plastic strain was 20%.

The plastic regime of the curve shows a region of very high work hardening rate up to 4% plastic strain followed by a region of lower strain hardening rates. The low strain/high work hardening region resembles the stage II of the shear stress-strain curves of single crystals and the high strain/low work hardening region resembles the stage III of the shear stress-strain curves of single crystals. The strain hardening rate at 200°C has been plotted as a function of strain level in Figure 4.28. This curve shows that the strain hardening rate continuously decreases with increasing strain levels. Strain hardening rate is very high up to nearly 4% plastic strain. Also, up to this strain level, the strain hardening rate decreases very fast. Strain hardening rate at 0.5% plastic strain was 1900 MPa which decreased to 700 MPa at 4% plastic strain. Beyond 4% plastic strain, the strain hardening rate is relatively low and also, the rate of decrease in strain hardening rate is low. The strain hardening rate decreases up to 200 MPa at 11% plastic strain. Above 11% plastic strain, strain hardening rate is very low and it remains nearly constant. The strain hardening rates observed in this study are in good agreement with those reported by Wasilewski et al.[36].

The four prestrain levels of 1%, 5%, 10%, and 15% plastic strain were employed prior to toughness testing. The specimen predeformed at 1% strain level had sufficient
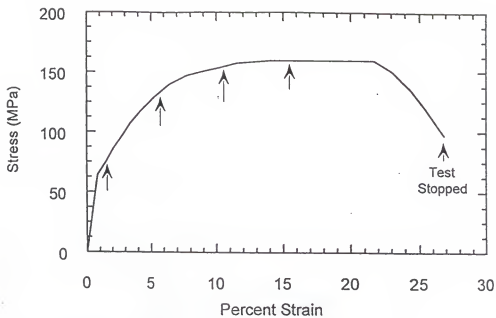
Figure 4.27 Engineering stress-strain curve at 200⁰C. The arrows show prestrain levels.
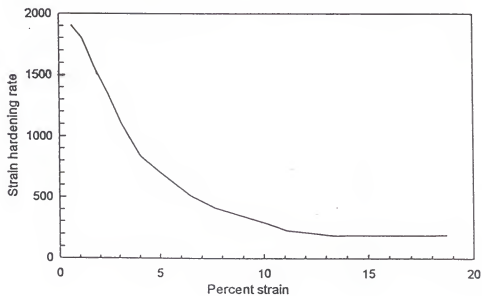

Figure 4.28 Strain hardening rate plotted as a function of strain at 200⁰C.

dislocation generation that resulted in the formation of barriers for dislocation motion by interlocking of dislocation networks. At 5% strain levels, more dislocations were generated, however, the high stress level achieved at this strain level was sufficient to overcome most of the barriers. At 10% strain level, a very low strain hardening rate indicates that most of the barriers were overcome. At 15% strain level, a constant strain hardening rate indicates that generation of new dislocations is being balanced by annihilation/recovery of dislocations occurring as a result of motion of dislocations.

4.3.2 Slip Trace Analysis

Slip trace analysis was performed on the specimens prestrained to 10% and 25% plastic strain levels. Figure 4.29(a) shows the duplex nature of slip traces along [0$\bar{1}$0] and [001] directions obtained on the (100) face of the specimen deformed to 25% plastic strain. At first, it appears that the slip markings should not be seen along [001] and [0$\bar{1}$0] directions on the (100) plane if <100> are the only possible slip directions because the resolved shear stress for the [100] slip direction is zero and [001] and [0$\bar{1}$0] directions lie in the (100) plane and hence should not be seen. One possible explanation is that these slip traces are the result of slight misorientation of the (100) face which would allow the [001] and [0$\bar{1}$0] displacement to be observed. It must be noted here that three of the possible slip planes viz. (001), (101) and ($\bar{1}$01) intersect with the observed (100) face along [0$\bar{1}$0] direction and similarly three other slip planes viz. (0$\bar{1}$0), (110), and ($\bar{1}$10) intersect with the (100) face along [001] direction. Therefore, in order to unambiguously determine whether the {100} or the {110} type slip planes have been activated, it was
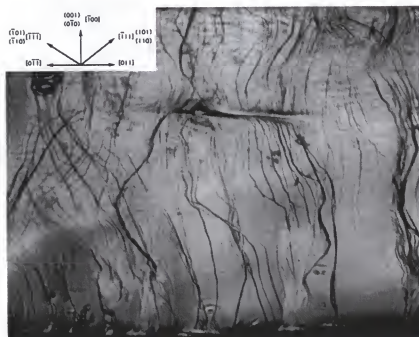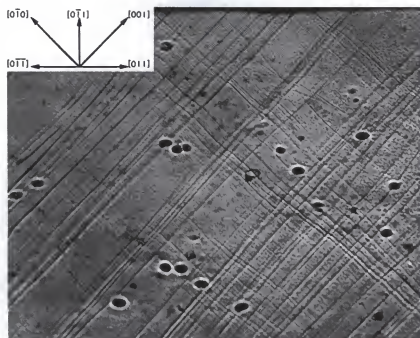
Figure 4.29 Slip traces observed at (a) (100) face, and (b) (011) face of a specimen deformed to 25% plastic strain level at 200°C. The tensile axis was [011].

necessary to look at the face perpendicular to the (100) face of the specimen. Microscopic observation of the (011) face [Figure 4.29(b)] showed the presence of slip markings along [100], [111] and [$\bar{1}$11] directions on this plane. This leads to the conclusion that slip systems activated after a 25% plastic strain include [0$\bar{1}$0](001), [001]($0\bar{1}0$), [001]($\bar{1}$10), [001](110), [010](101), and [0$\bar{1}$0](101). Slip traces were rather coarse and appeared to form large steps. The wavy nature of slip observed in Figure 4.29(b) suggests that the cross-slip between {001} planes and {110} planes had taken place. This observation suggests that the occurrence of the high strain rate low work hardening regime (stage III) is associated with cross-slip as a recovery process.

Slip traces observed on the specimen strained to 10% plastic strain are shown in Figure 4.30. In this case, duplex slip traces could be seen only near the edges on the (100) face of the specimen. This may be due to the fact that stresses are highest near the edges. The observation of (011) face of the specimen showed the presence of slip markings along [100] direction only. This suggests that only [0$\bar{1}$0](001), and [001]($0\bar{1}0$) slip systems were activated at this strain level. In addition, the observed slip traces were inhomogeneous. Slip traces could not be seen in the specimens deformed to lower strain levels. It should be noted that significant amount of slip along [010] and [101] is required to observe their traces at a shallow angle.

4.3.3 Effect of Prestraining on RT Fracture Toughness

Room temperature fracture toughness measurements were carried out on the prestrained specimens and results are shown in Table 4.13. The fracture toughness values
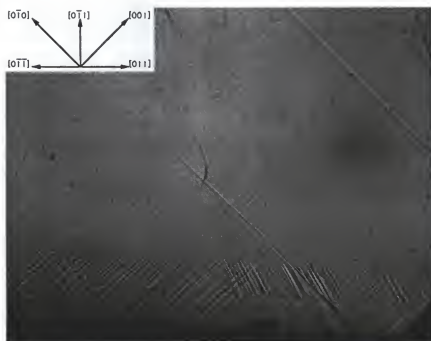
Figure 4.30 Slip traces observed in a specimen deformed to 10% plastic strain level at 200°C. The tensile axis was [011].

have been plotted as a function of the level of prestraining in Figure 4.31. The standard deviation of toughness data was 0.5 MPam$^{1/2}$. In general the fracture toughness of NiAl single crystal was increased upon prestraining. Initially, the fracture toughness increased significantly from 5.8 MPam$^{1/2}$ to 8.4 MPam$^{1/2}$, however, the rate of increase in fracture toughness decreased upon further prestraining. Fracture toughness of the specimen prestrained to 15% plastic strain was 9.5 MPam$^{1/2}$.

Table 4.13: Effect of prestraining on room temperature fracture toughness of NiAl single crystals.

Specimen Number	% Prestraining	K_{IC} (MPam$^{1/2}$)
D1	0	5.8
D4	0	5.9
D11	1	8.4
D9	5	8.6
D5	10	9.2
D8	15	9.5

4.3.4 Effect of Prestraining on BDTT

The BDTT was established for the specimens prestrained to 10% plastic strain level. 10% prestrain level was chosen for establishing the BDTT because at this strain level an extensive recovery of dislocations at 200^{0}C had not yet begun. Fracture toughness values of the as homogenized and the prestrained specimens at test temperatures are given in the form of J_{IC} and K_{IC} in Tables 4.14 and 4.15, respectively.
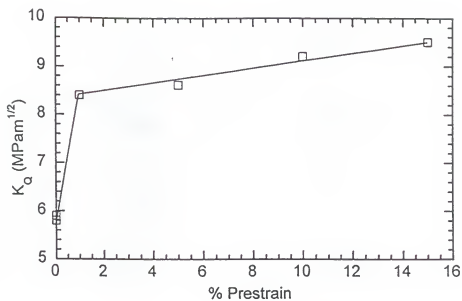
Figure 4.31 Room temperature fracture toughness of prestrained specimens as a function of prestrain level.
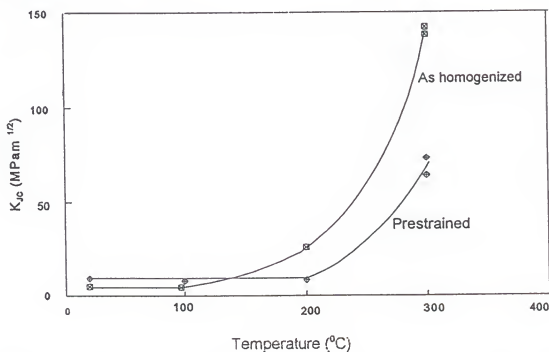

Figure 4.32 Brittle-to-ductile transition in the as homogenized and the prestrained crystal.

BDT curves for the as homogenized and the prestrained specimens are shown in Figure 4.32. A comparison of the BDT curves indicate that both types of specimens exhibit a gradual transition, however, the curve for the prestrained specimens is shifted towards higher temperatures. The fracture toughness of the prestrained crystal was nearly twice that of the as homogenized crystal at room temperature but it did not increase with temperature up to 200^0C. The fracture toughness of the as homogenized crystal increased gradually with increasing the temperature and at 200^0C the toughness of the as homogenized specimen was higher than that of the prestrained specimen.

The load-displacement curves obtained for both types of specimens at 200^0C are shown in Figure 4.33. The load-displacement curves show that the as homogenized specimen underwent the net-section yielding at 200^0C prior to fracture. The prestrained specimen, on the other hand, fractured within the linear elastic portion of the curve at 200^0C. Although the fracture load for the prestrained specimen was higher than that of the as homogenized specimen, its toughness was lower because the latter underwent the net-section yielding. Beyond this temperature, the fracture toughness of both types of specimens increased drastically.

The load-displacement curves for the prestrained and the as homogenized specimens at 300^0C are shown in Figure 4.34. The curves reveal that the prestrained specimen underwent the net-section yielding at 300^0C but it fractured at a lower displacement than the as homogenized specimen. The toughness of the prestrained specimen was much lower than that of the as homogenized specimen at 300^0C. The prestraining results have been analyzed in detail in section 5.2.

Table 4.14: Effect of prestraining on the BDTT as evaluated by K_{JC}.

Temperature (°C)	As Homogenized		Prestrained	
	K_{JC} (MPam$^{1/2}$)	Load-displacement behavior	K_{JC} (MPam$^{1/2}$)	Load-displacement behavior
20	5.0	Linear	9.2	Linear
100	4.6	Linear	7.9	Linear
100	5.0	Linear		
200	25.9	Non-linear	8.4	Linear
300	138.1	Non-linear	73.3	Non-linear
300	142.0	Non-linear	64.2	Non-linear

Table 4.15: Effect of prestraining on the BDTT as evaluated by J_{IC}.

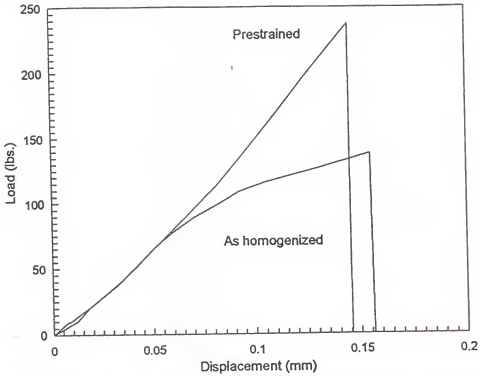| Temperature (°C)	As Homogenized		Prestrained	
	J_{IC} (KPam)	Load-displacement behavior	J_{IC} (KPam)	Load-displacement behavior
20	0.12	Linear	0.42	Linear
100	0.10	Linear	0.31	Linear
100	0.12	Linear		
200	4.0	Non-linear	0.35	Linear
300	114	Non-linear	32	Non-linear
300	120	Non-linear	25	Non-linear

Figure 4.33 A comparison of the load-displacement curves for the prestrained and the as homogenized specimen tested at 200°C.
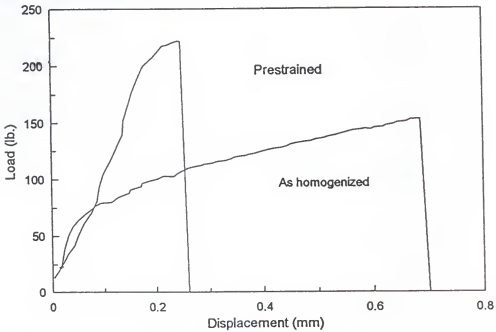

Figure 4.34 A comparison of the load-displacement curves for the prestrained and the as homogenized specimens tested at 300°C.

4.4 Toughness Anisotropy

Fracture toughness of NiAl single crystals is anisotropic in nature. Four point bend specimens of three different orientations were used to measure the toughness anisotropy. The results are shown in Table 4.16. The plane in the notation used to characterize the orientation in this table represents the plane of the notch whereas the direction represents the notch profile direction. As seen from the table, the toughness of $(101)[\bar{1}01]$ orientation was approximately twice the toughness of the $(100)[010]$ orientation.

Chang et al.[8] attributed this toughness anisotropy to the difference in the crack propagation path. In their study, the crack in the {100} orientated specimens kinked macroscopically into the {110} plane. They proposed that for the {100} specimens, the normal stress on the fracture plane, i.e., {110} reduced to half of the applied remote stress and , therefore, the toughness of {100} oriented specimens was approximately twice that of the {011} oriented specimens. The above proposition is based on the assumption that

Table 4.16: Toughness anisotropy in the as homogenized condition.

Specimen Number	Orientation	K_{IC} (MPam$^{1/2}$)
AB3	$(101)\ [\bar{1}01]$	5.6
AB8	$(101)\ [\bar{1}01]$	5.4
AB4	$(100)\ [010]$	9.2
EB1	$(100)\ [010]$	9.7
EB5	$(101)\ [010]$	7.9

the stress ratio ahead of a crack is similar to that for an un-notched specimen. This assumption may not be valid for the notched specimens where the stress distribution changes due to the presence of the notch. A rigorous analysis of elastic stresses for crack kinking by Palaniswamy and Knauss[75] suggests that the stress ratio for a kink angle of 45^0 is approximately 1.2 rather than 2. Another factor to consider is that the elastic modulus in the <100> direction is about half of that in the <011> direction[41] which under similar loading conditions would make the elastic energy release rate for the {100} plane to be eight times of that for the {110} plane. Considering that NiAl is a semi-brittle material, i.e., plasticity is a prerequisite for brittle crack initiation, the orientation dependence of toughness is expected to depend on the orientation dependence of plasticity also. Thus, the anisotropy in toughness for different notch planes appears to be a result of plastic anisotropy, elastic anisotropy and anisotropy due to different cleavage planes.

The results also show that the toughness depends on the plane of the notch and as well as on the direction of the notch profile. For a notch plane of (101), the toughness of the specimen having a [010] notch profile orientation was higher than those having a [$\bar{1}$01] notch profile orientation. The effect of the notch profile direction on fracture toughness is similar to the observations of Tsai and Mecholsky[76] on Si single crystals where they attributed the anisotropy in toughness to the anisotropy in elastic modulus.

4.4.1 Effect of Annealing of the Notch

Another set of experiments was conducted to study the effect of annealing of the notch on fracture toughness. This study was also performed on a GE crystal using the

four point bend specimens. In this study, the specimens of two orientations were heat treated at 1000°C for one hour and cooled under flowing argon. The two orientations were {101}<010> and {100}<010>. Some specimens were heat treated before making a notch while others were heat treated after making a notch using the EDM. The fracture toughness data obtained for the two orientations have been given in Table 4.17 and 4.18. The data show that the toughness increased significantly when the heat treatment was done after making a notch. However, the toughness did not change significantly when the same heat treatments were done prior to making a notch.

The toughness of (101)[010] oriented specimens was 7.9 MPam$^{1/2}$ in the as homogenized condition which increased to approximately 14 MPam$^{1/2}$ upon heat treating at 1000°C for one hour after making a notch. The toughness enhancement upon heat treatment was previously attributed to the unpinning of dislocations rendering them mobile[9]. However, the absence of toughness enhancement upon heat treating prior to

Table 4.17: Effect of heat treatments on the fracture toughness of (101) [010] oriented NiAl single crystal.

Specimen Number	Type of Heat Treatment	K_{IC} (MPam$^{1/2}$)
EB5	None	7.9
EB8	1000°C for 1 hour before making a notch	7.3
EB10	1000°C for 1 hour before making a notch	7.4
AB9	1000°C for 1 hour after making a notch	14.8
EB11	1000°C for 1 hour after making a notch	13.6

Table 4.18: Effect of heat treatments on the fracture toughness of (100) [010] oriented NiAl single crystals.

Specimen Number	Type of Heat Treatment	K_{IC} (MPam$^{\frac{1}{2}}$)
AB4	None	9.2
EB1	None	9.7
EB6	1000°C for 1 hour after making a notch	15.4
EB7	1000°C for 1 hour after making a notch	15.5

making a notch suggests that another mechanism may be operative in this case. Similar to the evaluation of fracture toughness of glasses using indentation flaws[77,78], the increase in toughness may be attributed to the relief of residual stresses and/or blunting of the sharp crack front produced by the EDM process. The residual stresses present ahead of the notch front alter the stress distribution and, therefore, result in different toughness values. The dislocation substructure produced during the notch making may recover upon heat treatment and, therefore, the residual stresses present ahead of the notch may change. The other possibility is that the sharp microcracks produced by the notch making process may get blunted during this heat treatment causing an "apparent" increase in toughness.

In the case of (100)[010] orientation, toughness increased from about 9.5 MPam$^{1/2}$ to about 15.5 MPam$^{1/2}$ upon heat treating the specimens in the notched condition. These results are consistent with those for the (101)[010] orientation.

4.5 Effect of Heat-Treatments on Fracture Toughness

Fracture toughness of single crystalline materials is very sensitive to the density of mobile dislocations. The density of mobile dislocations depends on the degree of pinning of dislocations. Dislocations can be pinned by point defects, viz., interstitial atoms, substitutional atoms, and vacancies as well as by other defects such as micro-voids, jogs, and clusters/precipitates. The degree of pinning of dislocations can be varied by varying the heat-treatment and cooling rates. The purpose of this part of the study was to employ a variety of heat-treatments and cooling rates to invoke various dislocation/point-defect interactions and to study their effect on fracture toughness.

The possible effects of heat-treatments are the following: (i) any residual stresses present in the specimen may get relieved, (ii) thermal vacancy concentration can be changed by changing the heat-treatment temperature and cooling rate, (iii) dislocations can be pinned and unpinned by interstitial and substitutional solutes depending on the temperature of heat-treatment and cooling rates, (iv) vacancies may form clusters and/or micro-voids depending on the heat-treatment temperature and cooling rates and these clusters/micro-voids may pin dislocations rendering them immobile, and (v) excessive vacancy concentration may lead to the formation of jogs on dislocations which impede the motion of dislocations.

Heat-treatments were also done after prestraining to study the effect of enhanced dislocation density on the above interactions. The details of various heat-treatments and their effects on fracture toughness have been described in this section.

One set of experiments was conducted using the double-notched tension specimens. This batch of specimens was cut from a GE crystal which had a fracture toughness of 7.8 MPam$^{1/2}$ in the as homogenized condition. Two temperatures, viz., 500^{0}C and 1200^{0}C were chosen for heat treatment and the specimens were cooled at two different cooling rates. These specimens were heat-treated in the notched condition. The 500^{0}C temperature was chosen because the equilibrium thermal vacancy concentration at this temperature is very low[40] and at the same time this temperature is high enough to remove the solute atmospheres around dislocations. The 1200^{0}C temperature was chosen because this temperature is expected to have a high thermal vacancy concentration[36]. The fracture toughness values obtained from heat treated specimens are given in Table 4.19. The specimen E13 which was heat treated at 500^{0}C for two hours and quenched to room temperature showed a toughness value similar to the as homogenized specimen. When a specimen was furnace cooled from 500^{0}C, the toughness was reduced to 5.9 MPam$^{1/2}$. The specimen which was heat treated at 1200^{0}C and water quenched to room temperature also showed a low toughness of 5.3 MPam$^{1/2}$. An intermediate cooling rate achieved by cooling under flowing argon from 1200^{0}C had insignificant effect on toughness (specimen E15).

The effect of heat treatments and cooling rates on fracture toughness can be explained by the effect of dislocation/point defect interactions. Following a heat treatment at 500^{0}C, specimens were cooled at two different cooling rates. The furnace cooled specimen had a toughness of 5.9 MPam$^{1/2}$, whereas the quenched specimen had a toughness of 7.9 MPam$^{1/2}$. It should be noted here that the standard deviation of

Table 4.19: Effect of heat treatments on room temperature fracture toughness of NiAl single crystals.

Specimen Number	Heat Treatment	K_{IC} (MPam$^{1/2}$)
E11	As received (argon filled vacuum furnace cooled from 1316°C)	7.8
E12	Heat treated at 500°C + slow cool	5.9
E13	Heat treated at 500°C + WQ to RT	7.9
E14	Heat treated at 1200°C + WQ to RT	5.3
E15	Heat treated at 1200°C + intermediate cool under argon flow	7.0

toughness data was 0.5 MPam$^{1/2}$, therefore, this difference in toughness is significant. This difference may be attributed to the fact that the very slow cooling rate allows sufficient time for the solutes to diffuse to dislocations and form an atmosphere around them. When a specimen was water quenched from 500⁰C, toughness did not change owing to the fact that interstitials did not get enough time to diffuse to dislocations. Also, quenching from 500⁰C did not alter the vacancy concentration significantly because the equilibrium vacancy concentration is very low at 500⁰C.

The specimen heat treated at 1200⁰C followed by water quenching to room temperature showed a toughness of 5.3 MPam$^{1/2}$ which is lower than the toughness of the as homogenized specimen. It is being speculated that this difference is due to the increased concentration of vacancies which was retained upon quenching. These vacancies are expected to increase the yield strength of the crystal and hence reduce the

toughness. It must be noted here that this specimen also showed a high concentration of large voids adjacent to the notch tip [see, section 4.6.2, Figure 4.49]. These voids could also contribute to the crack initiation process. The formation of voids ahead of the notch tip could be explained as follows: The residual stresses that are produced during the making a notch have a tensile hydrostatic component. The equilibrium concentration of vacancies is less under a hydrostatic stress state. The supersaturation of vacancies in this region results in their coalescence and formation of voids.

When a specimen was cooled at an intermediate rate from 1200^0C, the toughness values obtained were similar to those of the as homogenized specimen. This is due to the fact that this cooling rate was comparable to the cooling rate after the homogenization treatment. Whereas the specimen quenched from 1200^0C had a toughness lower than the toughness of the as homogenized specimen. These results also explain the differences in the fracture toughness of the as homogenized specimens from the GE crystal and the UF crystal. The GE crystal was cooled at a relatively faster cooling rate from the homogenization temperature. A faster cooling rate causes a vacancy concentration that is higher than the equilibrium concentration of vacancies at room temperature. These vacancies interact with dislocations and provide hardening.

Based upon these observations, it appears that a crystal cooled slowly from high temperatures up to 500^0C followed by quenching from 500^0C to room temperature will show a high fracture toughness.

4.5.1 Heat-treatment in the Prestrained Condition

Another set of experiments was conducted to study the effect of pinning of dislocations by interstitials in the prestrained condition. In this study, several heat treatments were carried in the specimens prestrained to 10% plastic strain. The data obtained is shown in Table 4.20. Based upon the Harper equation[79], the time required for 98% solutes to form an atmosphere around the dislocations was estimated to be 24 hours. Since the information regarding diffusivity and interaction energy of interstitials in NiAl is not available, the estimations were made by using the diffusivities of carbon in iron and also the interaction energy for the same. Specimens were cooled at different cooling rates from the prestraining temperature following the prestraining. The data show that the specimen water quenched to room temperature had a slightly higher toughness as compared with that of the specimen which was cooled under the flowing argon after prestraining. The aging at 200^0C for 24 hours after prestraining decreased the toughness of the prestrained specimen slightly. A slight decrease in toughness upon prestraining is attributed to a partial pinning of dislocations upon aging at 200^0C. It should be noted here that prestraining to 10% plastic strain level is expected to produce a large number of dislocations in the specimen and, thus, the interstitial concentration of the specimen may not be enough to form a solute atmosphere around all the dislocations. As a result, a large number of mobile dislocations were still available even after aging the specimen for such a long time. The availability of mobile dislocations may have been responsible for relatively high toughness values. Likewise, the slightly higher toughness values obtained

upon quenching the prestrained specimen from the prestraining temperature may have

been a result of the relatively less pinning of dislocations in this case as compared to the

furnace cooled specimen which allowed solutes to pin dislocations.

Table 4.20: Effect of heat treatments on toughness of the prestrained specimens.

Heat Treatment	K_{IC} (MPam$^{1/2}$)
As homogenized (cooled at 2.4°C/min from 1316°C)	5.8
As homogenized (cooled at 2.4°C/min from 1316°C)	5.9
10% prestrained at 200°C + WQ to RT	10.1
10% prestrained at 200°C + cooled under flowing argon	9.2
10% prestrained at 200°C + cooled under flowing argon	9.4

4.6 Fractography

The process of fracture comprises of two steps: (i) nucleation of crack, and (ii)

propagation of crack. It is, therefore, imperative to understand the nucleation and

propagation of crack as an effort to control the fracture toughness and the BDT. Fracture

surfaces of the tested specimens were analyzed for the crack nucleation and propagation.

Crack profiles were also analyzed by looking at the sides of the tested specimens. The

details of fractographic analysis have been presented in this section.

4.6.1 Crack Propagation

The crack propagation path was studied by analyzing the fracture surfaces as well as the crack profiles. Figure 4.35 shows the crack profile of a double-notched tension specimen tested at room temperature and at a loading rate of 10^{-2} mm/sec. The profile reveals that the fracture path did not follow the plane of the notch, instead the crack propagated at a plane inclined to the plane of the notch. As seen from this micrograph, the cleavage plane intersects with the (001) plane at 34^0 from the [$\bar{1}$10] direction. The analysis performed identified the trace to be [0$\bar{1}$5] which suggests that the cleavage plane is (511). This observation of {511} type cleavage planes is in agreement with previously reported results[8]. The fracture surface of the above specimen has been shown in Figure 4.36 (a) and (b). The fracture surface analysis [Figure 4.36 (b)] revealed that the cracking occurred by cleavage and that no microvoid coalescence was observed. The fractograph presented in Figure 4.36 (a) shows that the crack propagated at an angle to the notch plane of (110) as seen from the crack profile presented in Figure 4.35. However, the crack did not propagate completely on (511) plane. It is being proposed that the interactions of the crack with the stress field of the second notch resulted in the deflection of the crack and the crack went through a tortuous path towards the notch on the other side of the specimen. As seen in Figure 4.35 and also in Figure 4.37, the crack goes through a number of cleavage planes after being deflected. It should be noted here that there are twelve {511} planes and, therefore, the crack may traverse through a number of different {511} planes and also through other cleavage planes such as {110} and {100}.

Figure 4.35 Crack profile of a double-notched tension specimen tested at room temperature showing that the cleavage plane intersects along [$\bar{1}$50] with the (001) plane.
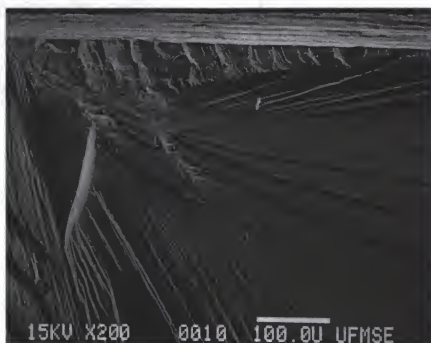
Figure 4.36 (a) Fracture surface of the specimen corresponding to the crack profile showing Figure 4.35. Figure 4.36 (b) A high magnification view of the fractograph shown in Figure 4.36 (a).
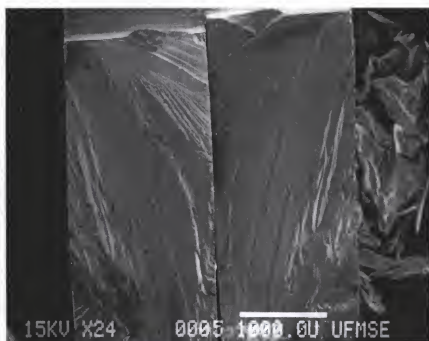
Figure 4.37 Fracture surface of a double-notched tension specimen showing multiple cleavage facets on the fracture surface.

Figure 4.38 shows a high magnification fractograph of the region marked by E in Figure 4.36(a). This fractograph shows the formation of a feature analogous to the "shear-lip" in steels. There are two possible mechanisms which may be responsible for the formation of "shear-lip" like features. One possibility is that the plane stress condition near the edge may enhance plasticity and change the fracture path analogous to shear-lips in metals capable of microvoid formation. The other possibility, however, is that these features may be a result of the formation of precracks during the introduction of the notch.

It was observed that the cleavage plane was independent of heat treatment and prestraining. The crack profile of a prestrained specimen has been shown in Figure 4.39. Figure 4.39 shows that similar to Figure 4.35, the crack propagates on the {511} plane. The specimen shown in Figure 4.35 was taken from a GE crystal which was heat treated prior to toughness testing and it had a fracture toughness of 5.3 MPam$^{1/2}$. The specimen shown in Figure 4.39 was taken from a UF crystal and was prestrained prior to toughness testing. This specimen showed a fracture toughness of 8.6 MPam$^{1/2}$. These observations seem to indicate that the crack propagation path at room temperature is not affected by prestraining and/or heat treatments in the case of double-notched tension specimens.

4.6.1.1 Effect of Loading Mode

The effects of loading mode on the fracture path was analyzed. The fracture paths of specimens loaded under four point bending have been shown in Figure 4.40 and 4.41. These fractographs correspond to the specimens having the same notch plane as used in
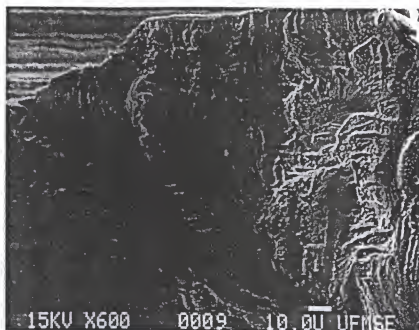
Figure 4.38 A high magnification fractograph of the area marked as E in Figure 4.36 (a).
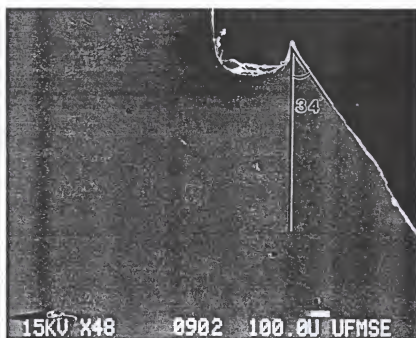
Figure 4.39 Crack profile of a prestrained specimen showing {511} cleavage facets similar to the non-prestrained specimen shown in Figure 4.35.
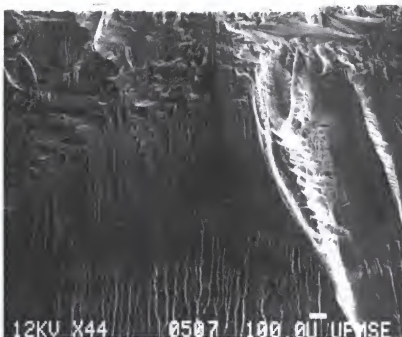
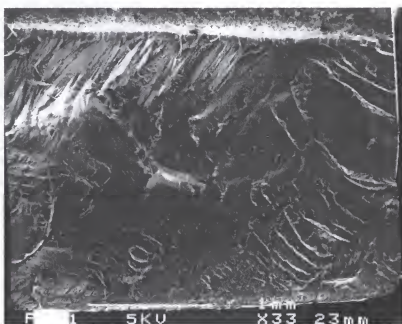Figure 4.40 Fracture surface of a four point bend specimen of {110}<010> orientation.

Figure 4.41 Fracture surface of a four point bend specimen of {110}<011> orientation.

the double-notched tension specimens. Contrary to the fracture surfaces of the double-notched tension specimens, the fracture surfaces were flat indicating a {110} cleavage. Chang et al.[8] analyzed fracture surfaces of four point bend specimens and observed the results similar to the present study where the cleavage plane was constrained to the {110} plane for the {110} oriented four point bend specimen. They observed {511} transient planes followed by {110} cleavage planes for the specimens having a {100} notch plane. Schneibel et al.[34] observed the occurrence of {511} and {711} cleavage plane in tensile specimens. The observations of the {511} cleavage plane in the case of double-notched tension specimens and {110} cleavage plane in the case of bend specimens of the same orientation in the present study clearly indicate that the cleavage plane depends on the loading mode in the case of NiAl single crystals.

4.6.1.2 Effect of Orientation

Fracture surfaces of the bend specimens having different orientations were analyzed. The fracture surface of a {110}<011> specimen has been shown in Figure 4.41. The fracture surface was macroscopically flat and the fracture plane was macroscopically confined to the notch plane of {011} for this orientation. However, in the {100}<010> specimen, the crack did not follow the {011} cleavage plane as shown by the fracture surface for this orientation in Figure 4.42. The crack profile from the mid-section of the specimen [Figure 4.43] suggests that macroscopically the crack followed the planes whose intersections with the (010) plane make 90^0 and 45^0 angles with the [100] direction. It should be noted here that the intersection trace does not constitute the
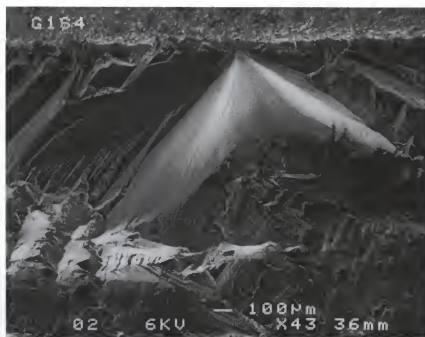
Figure 4.42 Fracture surface of a {100}<010> oriented four point bend specimen.

Figure 4.43 Crack profile of the specimen shown in Figure 4.42.

fracture plane, e.g., a comparison of Figures 4.42 and 4.43 demonstrates that a 45^0 profile angle does not imply a (101) fracture path. The overall profile angle depends on the relative size of the 45^0 and 90^0 segments. Microscopically the crack path consists of a three-dimensional sets of steps which accommodate an enforced macroscopic path. The microscopic segments are anticipated to be crystallographic, while the general macroscopic path may be governed by anisotropy of the elastic energy release rate.

In addition to the notch plane, the direction of the notch-front also had an effect on the fracture surface. This effect can be seen in Figures 4.40 and 4.41 which represent the fractographs {110}<010> and {110}<011> oriented bend specimens. As seen from the fractographs, both specimens exhibited a {110} cleavage plane, however, the directions of crack propagation were different.

4.6.1.3 Effect of Temperature and Displacement Rate

The fracture surface of the specimens tested over a range of temperatures and displacement rates were analyzed. The fracture surfaces showed that the fracture always occurred by cleavage mode and that no microvoid coalescence was observed in the displacement rate and temperature range studied. Macroscopic crack profiles appeared to be contained in the notch plane at higher temperatures and lower displacement rates. However, an examination of the fracture surfaces revealed that these fracture surfaces comprised of smaller cleavage facets and there were steps present between these cleavage facets. The fracture surfaces of specimens tested at 100^0C at the displacement rates of 2×10^{-4} mm/sec and 2×10^{-5} mm/sec have been shown in Figures 4.44-4.45.

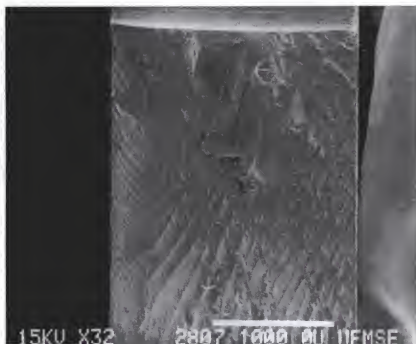Figure 4.44 Fracture surface of a double-notched specimen tested at 100°C at 2x10⁻⁴ mm/sec.

Figure 4.45 Fracture surface of a double-notched specimen tested at 2x10⁻⁵ mm/sec.

Although the fractographs appear to be macroscopically flat, they exhibit cleavage facets. A comparison of these micrographs shows that the size of the largest cleavage facet present on a fracture surface decreases with a decrease in strain rate. This indicates that there is a competition between cleavage and plasticity in these specimens. The crack tends to go through the cleavage plane but it gets arrested due to plasticity while the crack continues to propagate on other cleavage planes. This competition is manifested by the "stepped cleavage" as shown in these fractographs. At the faster displacement rate ($2x$ 10^{-4} mm/sec), the cleavage facets were present and they were larger as compared to those in the specimen tested at the slower displacement rate ($2x10^{-5}$ mm/sec). Similar results were shown at 200^0C. Fractographs of specimens tested at 10^{-2} mm/sec and $2x10^{-4}$ mm/sec at 200^0C have been presented in Figures 4.46 and 4.47 (a), respectively. The specimen tested at the slower displacement rate showed more plasticity and as a result, the cleavage facets were less evident on this specimen [Figure 4.47 (b)]. Similar results were obtained with increasing temperature. As the temperature increased, plasticity overcame the cleavage, which resulted in the formation of smaller cleavage facets. A comparison of Figures 4.44 and 4.47 which corresponded to the specimens tested at the same displacement rate and at 100^0C and 200^0C, respectively demonstrates that as the test temperature increased, the area of cleavage facets continued to decrease and the cleavage steps almost disappeared at 400^0C [Figures 4.48 (a) and (b)].
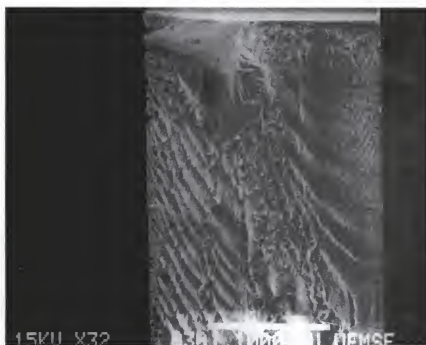
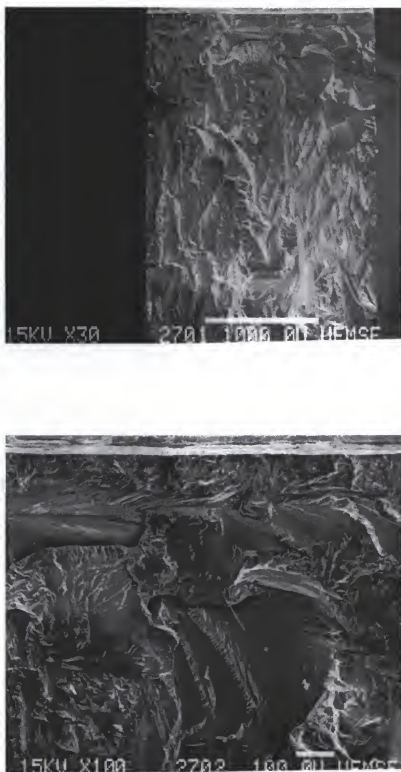Figure 4.46 Fracture surface of a double-notched specimen tested at 10^{-2} mm/sec.

Figure 4.47 (a) Fracture surface of a specimen tested at 200°C at 2×10^{-4} mm/sec, and (b) a high magnification view of the fracture surface shown in (a).
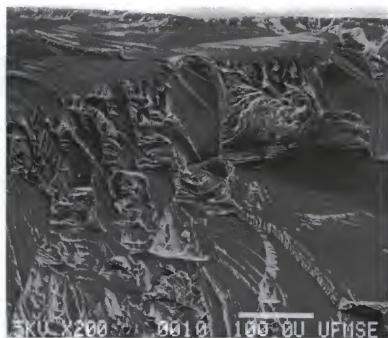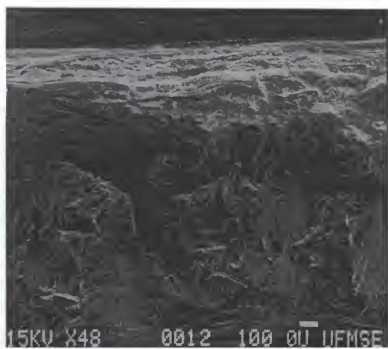
Figure 4.48 (a) SEM fractogtaph of a specimen tested at 400°C at 10^{-2} mm/sec, and (b) a high magnification view of the fracture surface shown in (a).

4.6.2 Crack Nucleation

In order to study the mechanism of crack nucleation, one specimen of the double-notched-tension geometry was partially loaded at 350^0C and unloaded prior to fracture. The sides of this specimen were examined under the scanning electron microscope for microcracking. Microcracks of 1-2 μm size were observed adjacent to the notch tip. These microcracks have been shown at different magnifications in Figure 4.49 (a)-(c). These microcracks were not present in the specimen prior to loading. As seen from these micrographs, the microcracks nucleated along the slip bands adjacent to the notch tip during loading. Slip traces in the same specimen were observed more clearly under an optical microscope. Optical micrographs showing the slip traces in the same region of the same specimen are shown in Figure 4.50 (a) and (b). Slip started to occur ahead of the notch tip in the plastic zone. The area showing slip traces grew as the plastic zone grew with increasing load. Figure 4.50 (a) shows a zone having a shape of small triangle marked by an arrow. A higher magnification micrograph of the zone A has been shown in Figure 4.50 (b). This is a zone of intense slip near the notch tip. Since the localization of strain occurs along the slip bands ahead of the notch tip, it appears from these micrographs that localization of strain may be responsible for the nucleation of crack in NiAl single crystals.

Another specimen tested at 400^0C up to the unstable fracture was also analyzed for secondary cracks. The sides of the specimen had a number of shear cracks present along the slip bands. These cracks and the slip bands are shown in Figures 4.51. Since the
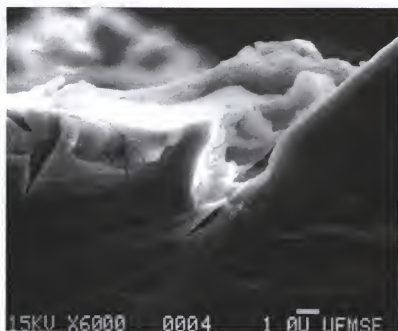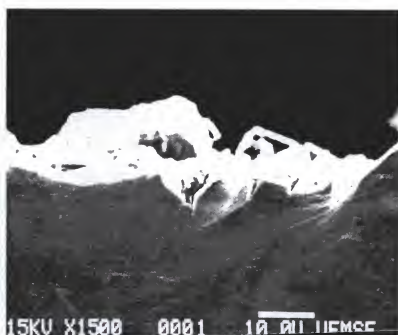
Figure 4.49 (a) SEM micrograph showing the microcracks present ahead of the notch in a partially loaded specimen, (b) and (c) High magnification SEM micrographs showing the microcracks present along slip bands in a partially loaded specimen.
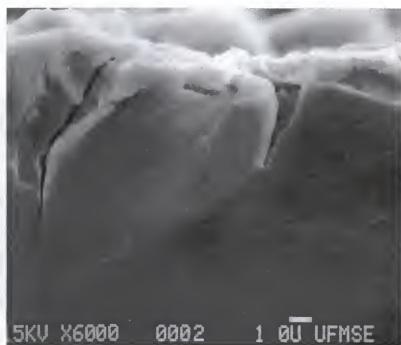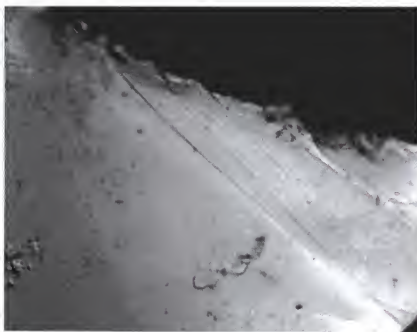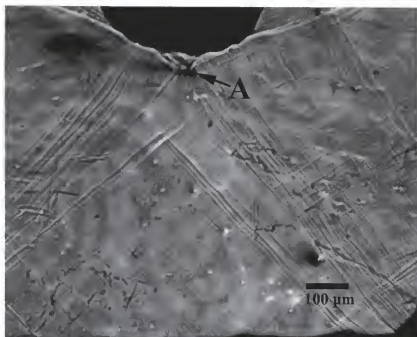
Figure 4.49--continued

Figure 4.50 (a) An optical micrograph showing the slip bands in the plastic zone of a partially loaded specimen. (b) An optical micrograph showing the area of intense slip ahead of the notch (marked by A in Figure 4.50a).
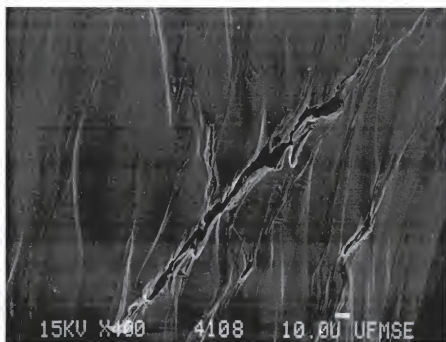
Figure 4.51 SEM micrograph showing the presence of the shear cracks in a specimen tested at 400°C.

specimen tested at 400⁰C underwent severe plastic deformation prior to fracture, the slip

traces observed in this specimen were very deep. As a result, slip traces could be seen

more clearly in this specimen under the scanning electron microscope. The cracks seen in

Figure 4.51 are secondary cracks that did not go unstable during the test. However, these

micrographs support the observations made from Figure 4.46 that cracks initiated along

the slip bands.

In one specimen, which was heat treated at high temperature followed by

quenching in water, voids similar to the ones shown in Figure 4.52 (a) and (b) were found

near the notch tip. It is being speculated that the formation of these voids occurred due to

a high vacancy concentration resulting from the heat treatment at high temperature. These

voids may contribute to the crack nucleation process by providing crack nuclei.

The crack nucleation sites can often be identified rather distinctly on most of the

fracture surfaces. A flat initiation zone (marked by A on the micrograph) similar to the

"mirror" region in the fracture of brittle materials is shown in Figure 4.53. The zone

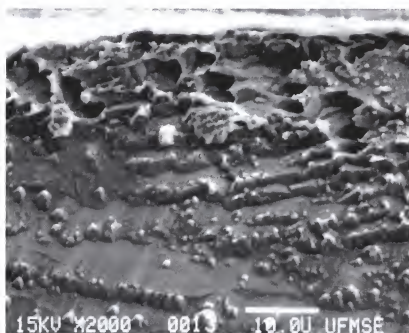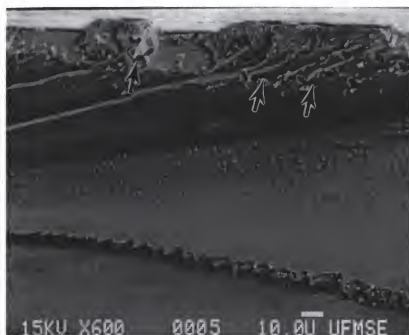corresponds to the nucleation of crack prior to its unstable propagation.

Figure 4.52 (a) and (b) SEM micrographs showing voids present near the notch tip of a quenched specimen at different magnifications.
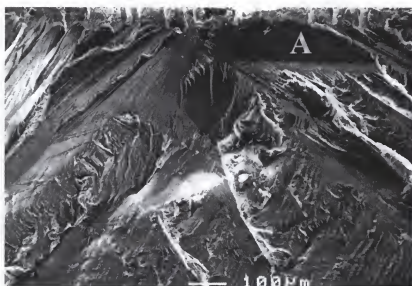
Figure 4.53 A fractograph showing a distinct crack initiation zone analogous to the "mirror" region in the fracture of brittle materials.

CHAPTER 5
GENERAL DISCUSSION

The main issues that remain to be addressed are: what are the processes responsible for the BDTT in NiAl and why does the prestraining increase the BDTT while it increases the room temperature toughness? In this chapter we will examine the mechanism of the BDT and analyze the effects of prestraining on room temperature toughness and on the BDTT.

5.1 BDTT

The fracture process comprises of two steps, viz., nucleation of a crack and unstable propagation of a crack. Crack instability is either "nucleation-controlled"or "propagation-controlled" depending on the temperature. At low temperatures, the crack instability is "nucleation-controlled" where the unstable fracture occurs as soon as a microcrack is nucleated. At high temperatures, the crack instability is "propagation-controlled" where stable microcracks may exist. At these temperatures, the fracture does not occur immediately after the nucleation of a microcrack and many stable microcracks develop prior to the unstable crack propagation. The occurrence of stable microcracks similar to those shown in Figure 4.49 [section 4.6.2] suggests that this mechanism is operative in the case of NiAl single crystals at temperatures above the BDTT. As

described in section 4.6.2, the localization of strain is responsible for crack nucleation in NiAl single crystals.

As shown in Figure 2.5, the stress distribution ahead of a crack depends on the yield strength as well as on the strain hardening exponent. In a simplistic view, the unstable propagation of the crack occurs when the stress near the crack tip becomes higher than the critical fracture stress over a critical length. The fracture stress is considered to be nearly temperature independent. As described in section 4.1, the yield strength and the strain hardening exponent both are dependent on temperature and strain rate in NiAl single crystals. At low temperatures and high displacement rates, the yield strength and the strain hardening exponent are high causing very high stresses near the crack tip. Thus, fracture stress is achieved at low remote applied stress levels. At higher temperatures and lower loading rates, the yield strength and strain hardening exponent are low and thus, the stresses near the crack tip are not as high. As a result, the remote applied stress has to be very high in order to achieve a stress equivalent to the fracture stress near the crack tip. This results in higher toughness values at lower displacement rates and higher temperatures.

As the temperature is increased, the plastic flow of the material is facilitated causing the occurrence of the net-section yielding before the stress distribution ahead of the notch can cause an unstable fracture. As a result of the net-section yielding, the plastic constraint is lost and stresses are no longer concentrated at the crack tip. Then the question arises as to what facilitates the plastic flow above the BDTT. Is it due to the fact that the dislocation nucleation becomes easier above this temperature or due to the fact

that dislocation motion is facilitated above this temperature? If the BDTT was limited by the generation of nucleation (as may be the case of other single crystals such as Si), generating more dislocations by prestraining would have decreased the BDTT. But, the results shown in section 4.3 indicate that the BDTT does not decrease by increasing the dislocation density in NiAl single crystals. Therefore NiAl single crystals do not exhibit a "dislocation density controlled" BDT.

The other possibility, then, is that the motion of dislocations above the BDTT is facilitated causing the plastic flow of the material in the crack tip region. The activation energy for the BDT was found to be in agreement with the activation energy of the thermally activated tensile deformation within the same temperature range. This supports that thermally activated plastic flow is responsible for the BDT in NiAl single crystals. The motion of dislocations can be facilitated in one or more of the following ways: (i) thermally assisted processes such as cross-slip and climb of dislocations become operative at and above this temperature, and/or (ii) other slip systems become operative near this temperature. The occurrence of other slip systems has been reported in NiAl[2], but, at temperatures much higher than the observed BDTT. In this study, slip trace analysis of tensile and fracture specimens has shown that slip is limited to <100> displacement vector, however, cross-slip occurs at elevated temperatures and large applied strains. Therefore, the possibility that the occurrence of other slip systems is responsible for the BDT is precluded.

The activation energy for climb of dislocations at $T > 0.5 \, T_m$, where T_m is the melting point, has been shown to be equal to the activation energy for self diffusion in

many metals and alloys[80,81]. However, for intermetallics and non-metallic compounds, it has been shown that a small deviation from stoichiometry can significantly reduce the activation energy for climb[80]. The activation energy values calculated in this study (48-84 KJ/mole) are much lower than the activation energy values reported for diffusion (197 KJ/mole) in NiAl. This inconsistency may be associated with the existence of a high constitutional vacancy concentration in the crystal tested. Another possibility is that cross-slip of {100} dislocations to {0kl} planes (pencil glide) may be sufficient for facilitating the deformation and the activation energy is related to the process of cross-slip.

5.2 Prestraining

One possible reason of increased room temperature toughness upon prestraining could be a change of fracture path in prestrained specimens. The analysis of the fracture surfaces and crack profiles [see, section 4.6.1] of the tested specimens showed that the fracture path was not affected by prestraining. The crack profiles of the prestrained and "non-prestrained" specimens can be compared by looking at Figures 4.35 and 4.39. As shown in these figures, both specimens show a {511} cleavage plane. This observation precluded the possibility that the increased toughness was a result of change in fracture path.

Prestraining has been reported to increase the fracture toughness of Si, Ge, and MgO single crystals[62]. Hirsch and Roberts[59] attributed the increase in toughness to the shielding of the crack tip by dislocations. According to a model proposed by them[59], the

dislocations emitted from sources at or near the crack tip cause shielding of the crack tip, which lowers the local stress intensity at the crack tip. In this model, the effective local stress intensity (K_{eff}) is given by:

$$K_{eff} = K - \Sigma K_d \qquad (5.1)$$

where K is the applied stress intensity factor and K_d is the stress intensity factor due to each dislocation. K_d varies inversely as the square root of the distance between the crack tip and each dislocation. Thus the local stress intensity of the crack tip may be reduced by the presence of dislocations leading to an increase in toughness. The observations of the effect of prestraining on increasing the room temperature fracture toughness of NiAl single crystals in the present investigation are in agreement with the above model. However, the above model does not explain the observed effects of prestraining on increasing the BDTT in NiAl single crystals. Hirsch and Roberts model[59] predicts that prestraining decreases the BDTT in single-crystalline materials such as Si and MgO. However, these single crystals have a very low dislocation density and a very high yield stress. The yield stress of NiAl is relatively lower and, therefore, the above model may not be applicable in this case.

Ashby and Embury[64] used a simple model to show how dislocations multiply and act as a source, when dislocation density is high. According to this model, plasticity and blunting of the crack tip may be prevented simply because the nearest dislocations are too far away. At low dislocation densities, the crack tip field is insufficient to move and multiply dislocations, and as a result, dissipation of energy and blunting of the crack tip

does not occur. At higher dislocation densities, dislocations lie closer to the crack tip; then the lattice resistance is exceeded by the crack tip field and dislocations move and multiply, dissipating energy and blunting the crack tip. They predict that the BDTT should decrease slowly as the dislocation density is increased up to a density of 10^{13} cm^{-2}. The model further predicts that the BDTT increases with an increase in dislocation density beyond 10^{13} cm^{-2}. The results of the model have been shown in Figure 2.10 (b). The model predicts that when the work hardening contribution to local flow stress becomes larger than the effect of plasticity and blunting, the BDTT increases rapidly as the dislocation density increases. Thus, Ashby and Embury model can explain the increase in the BDTT of NiAl single crystals upon prestraining.

At first, the effects of prestraining on increasing the room temperature toughness and on increasing the BDTT seem to be contrary to each other. However, a careful look at the BDT mechanism explains this behavior. Based upon the BDT mechanism suggested in section 5.1, the toughness at lower temperatures can be increased by decreasing the possibility of the nucleation of a crack whereas the toughness at higher temperatures can be increased by hindering the unstable propagation of the crack. The following scheme based on the localization of strain explains how the prestraining influences the nucleation of the crack in the low temperature regime and the propagation of the crack in the high temperature regime.

In general the fracture toughness is controlled by the combination of microcrack distribution and stress distribution in the vicinity of the notch. At low temperatures where the fracture is "nucleation-controlled", an increased dislocation density can increase

toughness by decreasing the possibility of microcracking. Prestraining increases the number of dislocation sources. An increased density of dislocation sources reduces the localization of strain by allowing the slip to occur more uniformly near the notch. As shown in Figure 4.49 [section 4.6.1], microcracking in NiAl occurs on slip bands that form at the notch tip suggesting that slip localization is responsible for the crack initiation in NiAl single crystals. Thus, a reduced localization leads to a difficulty in the nucleation of microcracks ahead of the notch. It must be noted here that the prestraining also increases the flow stress of the material. However, in the case of room temperature toughness tests, the above effect overcomes the effect of enhanced flow stress and an increase in toughness is observed.

The increase in the BDTT of NiAl due to prestraining can be attributed to the increase in yield strength. As shown in Figure 4.34, the prestrained specimen showed a much higher load at the net-section yielding at 300^0C test temperature than did the as-homogenized specimen. Considering that the fracture is "propagation-controlled" at elevated temperatures, an increase in yield strength which raises the stress distribution ahead of the notch leads to a lower toughness value for the prestrained crystal. In other words, the prestrained specimen attained similar stress distributions ahead of the notch at a smaller remote displacement as compared to the as-homogenized specimen.

CHAPTER 6
CONCLUSIONS

The BDTT of NiAl single crystals was established by conducting fracture toughness tests using the double-notched tension specimens of {110} orientation. The BDTT was found to vary in the range of below room temperature to 200^0C depending upon the applied displacement rate. It was proposed that the crack instability at temperatures below the BDTT is "nucleation-controlled" whereas the crack instability at temperatures above the BDTT was "propagation controlled". The crack nucleation mechanism in NiAl single crystals was established experimentally. A partial loading and a subsequent unloading prior to the fracture revealed the nucleation of microcracks along slip bands in the crack tip region. This suggested that the localization of strain is responsible for crack nucleation in NiAl single crystals. Crack propagation paths of the tested specimens were studied. It was observed that the cleavage occurred in NiAl single crystals along {511} planes for the geometry and orientations used in the study. The observation of {511} cleavage planes is in agreement with the previously reported results. The cleavage plane was found to be independent of heat treatment, prestraining, and temperature. However, the size of the largest cleavage facet decreased with increasing temperature.

Prestraining was performed at elevated temperatures under tension and its effect on the BDTT was established. It was found that the BDTT of the NiAl single crystals increases upon prestraining. This was attributed to an increase in yield strength upon prestraining. The increased yield strength facilitates the unstable propagation of cracks at lower applied displacements. The increase in the BDTT upon prestraining suggested that the BDT of NiAl single crystals in not limited by the dislocation density. Prestraining was found to increase the room temperature fracture toughness from 5.8 MPam$^{1/2}$ to 9.5 MPam$^{1/2}$. This was attributed to the reduced localization of strain achieved due to the enhanced dislocation density upon prestraining. Different levels of prestraining were used to study the effect of the prestraining level on toughness. A slight effect of the prestraining level on toughness was obtained. Higher prestrain levels resulted in higher fracture toughness values.

The activation energy associated with the BDT was estimated based upon the experimental data. The activation energy for the BDT of NiAl single crystals was found to be 48.4 KJ/mole. Based upon the tensile data, the activation energies for thermally assisted deformation were also calculated as a function of applied stress level using a model proposed by Reed-Hill et al[70]. The activation energy for the BDT compared well with the activation energy obtained by Reed-Hill model for an applied stress level of 100 MPa. This indicated that thermally assisted plastic deformation that occurs at the notch tip prior to the onset of unstable fracture is responsible for the BDT in NiAl single crystals.

Tensile properties were obtained as a function of temperature and strain rate. The yield strength and the strain hardening exponent both were found to be dependent on the

strain rate and temperature. While the strain rate dependence of the yield strength is typical of BCC metals, a drastic increase in strain hardening rate with increasing temperature and decreasing strain rate indicated a behavior similar to HCP and FCC metals.

The fracture toughness of NiAl single crystals was found to be very sensitive to heat treatments. The observed effects of heat treatments on fracture toughness as well as the analysis of tensile properties as a function of temperature and strain rate indicated the occurrence of strain aging in NiAl single crystals.

LIST OF REFERENCES

1. R. Darolia in Structural Intermetallics, eds. R. Darolia, J.J. Lewandowski, C.T. Liu, P.L. Martin, D.B. Miracle, and M.V. Nathal, The Minerals, Metals, and Materials Society (1993) 495.

2.. D.B. Miracle, Acta Metall. Mater., 41(3) (1993) 649.

2. R.D. Noebe, R.R. Bowman, and M.V. Nathal in Physical Metallurgy and Processing of Intermetallic Compounds, eds N.S. Stoloff, and V.K. Sikka, Van Nostrand Reinhold, New York (1993).

4. R. Darolia, J. Of Metals, 43(3) (1991) 44.

5. D.B. Miracle and R. Darolia in Intermetallic Compounds: Principals and Practice, Eds. J.H. Westbrook and R.L. Fleischer, John Wiley and Sons, New York (1993).

6. W.S. Walston and R. Darolia in High Temperature Ordered Intermetallic Alloys V, eds. I. Baker, R. Darolia, J.D. Whittenberger and M.H. Yoo, Materials Research Society, Pittsburgh, 288 (1993) 237.

7. R.D. Noebe, C.L. Cullers, and R.R. Bowman, J. Mater. Res., 7(3) (1992)605.

8. K.M. Chang, R. Darolia and H.A. Lipsitt, Acta Metall. Mater., 40 (10) (1992) 2727.

9. J.E. Hack, J.M. Brzeski and R. Darolia, Scipta Metall. Mater., 27 (1992) 1259.

10. G.Bergmann and H. Vehoff, Scripta Metall. Mater., 30 (8) (1994) 969.

11. S. Shrivastava and F. Ebrahimi, Proceedings of Materials Research Society 364, (1994) 431.

12. S. Shrivastava and F. Ebrahimi, Accepted for publication in Proceedings of Materials Research Society, (1996).

13. V.I. Levit, I.A. Bul, J. Hu and M.J. Kaufman, Scripta Mater., 34 (12) (1996) 1925.

14. M.L. Weaver, M.J. Kaufman and R.D. Noebe, Met. Trans.A, 27 (2) (1996) 1.

15. A. Wolfenden, S.V. Raj and S.K.R. Kondlapudi, J. Mater. Res., 9 (5) (1994) 1166.

16. C. St. John, Philos. Mag., 32 (1975) 1193.

17. A.G. Fox and M.A. Tabernor, Acta Metall. Mater., 39 (1991) 669.

18. H. Hang and W.W. Gereberich, Acta Metall. Mater., 43 (1994) 639.

19. R.D. Noebe, R.R. Bowman and M.V. Nathal, Int. Mater. Rev. 38 (1993) 193.

20. R.E. Reed-Hill and T. Zhu, High Temperature Materials and Processes, 6, 93 (1984).

21. C.G. Kallingal, T.R. Smith, N.S. Stoloff and K. Rajan, Acta Metall. Mater., 42 (11) (1994) 3731.

22. R.D. Field, D.F. Lahrman and R. Darolia, Acta Metall. Mater., 39 (12) (1991) 2951.

23. A. Ball and R.E. Smallman, Acta Metall. Mater., 14 (1966) 1349.

24. A. Ball and R.E. Smallman, Acta Metall. Mater., 14 (1966) 1517.

25. M. H. Loretto and R.J. Wasilewski, Phil. Mag. 23 (1971) 1311.

26. D.F. Lahrman, R.D. Field and R. Darolia in High Temperature Intermetallic Alloys V, eds. I. Baker, R. Darolia, J.D. Whittenberger and M.H. Yoo, Materials Research Society, Pittsburgh, PA (1993) 45.

27. K.R. Frobes, U. Glatzel, R. Darolia and W.D. Nix in High Ztemperature Ordered Intermetallic Alloys V, eds. I. Baker, R. Darolia, J.D. Whittenberger and M.H. Yoo, Materials Research Society, Pittsburgh, PA (1993) 45.

28. I. Baker, Materials Science and Engineering, A192/193 (1995) 1.

29. M. Saeedvafa and J.R. Rice, Modelling Simul. Mater. Sci. Eng., 1 (1992) 53.

30. T. Takashugi, S.Watanabe and S. Hanada, Mat. Sci. & Engg., A149 (1992) 183.

31.   C.P. Blankenship, Jr., M. Larsen, and J.A. Sutliff, Acta Metall. Mater., 43 (4) (1995) 1549.

32.   K. Yoshimi, S. Handa, and M.H. Yoo, Acta Metall. Mater., 43 (11) (1995) 4141.

33.   R.J. Wasilewski, S.R. Butler, and J.E. Hanlon, Transactions of the Metallurgical Society of AIME, 239 (9) (1967) 1357.

34.   J.H. Schneibel, R. Darolia, D.F. Lahrman and S. Schmoauder, Met Trans. A, 24A (1993) 1363.

35.   C.K. Hong and P.R. Monroe, Intermetallics, 2 (1994) 333.

36.   R.J. Wasilewski, Acta Metall., 15 (1967) 1757.

37.   W. Yang, R.A. Dodd and P.R. Strutt, Met. Trans., 3 (1972) 2049.

38.   W.J. Yang and R.A. Dodd, Scripta Metall., 8 (1974) 237.

39.   J.E. Eibner, H.J. Engell, H. Schultz, H. Jacobi, and G. Schlatte, Phil. Mag., 39 (1975) 739.

40.   N. Rusovic, E.T. Henig, Phys. Stat. Sol., A57 (1980) 529.

41.   J.E. Epperson, K.W. Gerstenberg, D. Berner, G. Kostorz, and C. Ortiz, Phil Mag., A38 (1978) 529.

42.   K. Vedula and P.S. Khadkikar in High Temprature Aluminides and Intermetallics, S.H. Wang, C.T. Liu, D.P. Pope and J.O. Stiegler, eds. TMS, Warrendale, PA, (1990) 197.

43.   Y.J. Lim, K.T. Hong, V. Levit and M.J. Kaufman, MRS Proc. 364 (1995) 273.

44.   A.J. Duncan, Ph.D. dissertation, University of Florida (1995).

45.   M.L. Weaver, Ph.D. dissertation, University of Florida (1994).

46.   A.A. Griffith, Phil. Trans. Roy. Soc., A221 (4) (1920)163-168.

47.   C.E. Inglis, Trans. Int. Naval Archit., 55 (1913) 219.

48.   G.R. Irwin, Fracturing of Metals, ASM, Cleveland, OH (1949).

49.   H.W. Westergaard, Trans. ASME, J. Appl, Mech., 61 (6) (1939) A49-53.

50.   J.R. Rice, J. Appl. Mech., (1968) 379-386.

51.   D.S. Dugdale, J. Mech. Phys. Sol., 8 (1960) 100.

52.   D.G.H. Latzko, Post Yield Fracture Mechanics, Applied Science Publishers
       Limited, New York (1979).

53.   D.A. Curry and J.F. Knott, Metal Science, 13 (1979) 341.

54.   R.O. Richie, J.F. Knott and J.R. Rice, J. Appl. Phys. Sol., 21 (1973) 395.

55.   J.R. Rice and M.A. Johnson, Inelastic Behavior of Solids (ed. M.F. Kanninen, W.
       Adler, A. Rosenfield, and R. Jaffe), McGraw Hill, New York (1970) 641.

56.   J.W. Hutchinson, J. Mech. Phys. Solids, 16 (1968) 13.

57.   J. R. Rice and G.F. Rosengren, J. Mech. Phys. Solids, 16 (1) (1968) 1.

58.   S.G. Roberts , A.S. Booth and P.B. Hirsch, Mat. Sci. Engg., A176 (1994) 91.

59.   P.B. Hirsch and S.G. Roberts, Philo. Mag., 64 (1991), 55.

60.   S.G. Roberts, M.Ellis and P.B. Ellis, Materials Science and Engineering, A164
       (1993) 135.

61.   P.D. Warren, Scripta Met. Mat., 23 (1989) 637.

62.   P.B. Hirsch and S.G. Roberts, Scripta Metall. Mater., 23 (1989) 925.

63.   J.R. Rice and R. Thomson, Phil. Mag., 23 (1974) 73.

64.   M.F. Ashby and J.D. Embury, Scripta Metall. Mater., 19 (1985), 557.

65.   M. Kantha, D.P. Pope and V. Vitek, Scripta Metall. Mater., 31 (10) (1994) 1349.

66.   ASTM Standards E399, 03.01 (1992).

67.   D. Broek, Elementary Engineering Fracture Mechanics, Kluwer Academic
       Publishers New York(1986).

68.   O.L. Towers, NBS Report No. 7709.01.81/249.1 (1981).

69.   R.W. Hertzberg, Deformation and Fracture Mechanics of Engineering Materials, John Wiley & Sons, New York, (1989).

70.   R.E. Reed-Hill, C.V. Iswaran and M.J. Kaufman, Scripta Mater., 33 91) (1995) 157.

71.   R.E. Reed-Hill and M.J. Kaufman, Acta Metall. Mater., 5 (1995) 1731.

72.   C.V. Iswaran, R.E. Reed-Hill V.I. Levit and M.J. Kaufman, Scripta Metall. Mater., 32 (7) (1995) 941.

73.   G.F. Hancock and B.R. McDonnell, Physica Status Solidi (a), 4 (1971) 143.

74.   S. Shankar and L.L. Seigle, Metall. Trans., 9A (1978) 1467.

75.   K. Palaniswamy and W.G. Knauss, in Mechanics Today, S. Nemat-Nasser, Ed., 4 Pergamon Press (1978) 87.

76.   Y.L. Tsai and J.J. Mecholsky, Jr., J. Mater. Res., 6 6) (1991) 1248.

77.   B.R. Lawn, K. Jakus and A.C. Gonzalez, J. Am. Cer. Soc. 70 (6) (1987) 377.

78.   K. Hirao and M. Tomazawa, Scripta Metall. Mater. 30 (1994) 969.

79.   S. Harper Phys. Rev., 83 (1951) 709.

80.   Metals Handbook, American Society of Metals, Metals Park , OH, 12 (1994).

81.   W.J. McGregor Tegart, Elements of Mechanical Metallurgy, McMillan, New York, 1966.

APPENDIX A
EFFECT OF NOTCH-TYPE ON FRACTURE TOUGHNESS

The standard techniques for evaluating the fracture toughness of metals and intermetallics involve tests on notched specimens. Various techniques to introduce a starter crack in these specimens include fatigue precracking and preparing a notch using the electric discharge machine (EDM), diamond saw or wire saw. The fatigue cracking process results in a sharp natural crack but it is a time consuming process where there is less control on the size and orientation of the initial crack. Fatigue cracking also adds to the cost and complexity of conducting fracture tests. For the above reasons, efforts have been made to be able to produce an ideal, sharp machined notch, where a control over the orientation, shape and size of the initiator crack could be obtained. Prior to adopting notches introduced by using the diamond saw, two types of notches, viz., those introduced by the EDM and those by the diamond saw were evaluated.

The EDM notches were found to create significant surfaces damage in the area near the notch. The damage created by the EDM notch has been shown in Figure A-1. This micrograph was taken by introducing a notch on an electropolished specimen and characterizing it. In this micrograph, a distinct region can be seen near the notch front. This region consists of the material which was melted during the cutting and solidified after the cutting. Patches of the re-solidified material can be seen. Also, the EDM process

results into cracking ahead of the notch. These cracks have been shown in Figure A-2. These cracks were seen on the fracture surfaces of tested specimens as a zone containing accordion-shape planes. These cracks had a length of about 30-50 μm and were present between the fracture initiation site and the notch tip [Figure A-3]. It was proven that these planes were present prior to loading the specimen and that they were not created during loading in the following way: When the specimens were heat treated in the notched condition prior to loading, the fracture surfaces of tested specimens showed similar planes but in an oxidized condition. The oxidized accordion-shape planes have been shown in Figure A-4. The formation of these cracks was attributed to the solidification shrinkage following the localized melting caused during the EDM cutting.

The toughness values obtained from the specimens containing the EDM notches compared well with those containing the diamond saw notches. However, the diamond saw notches did not cause such a severe damage near the notch as the EDM notch. Two specimens containing EDM and diamond saw notches were etch pitted to see the dislocations created by each type of the notch during the process of introduction of the notch. The etch pitted regions of the two notches have been shown in Figures A-5 and A-6. These figures indicate that the specimens containing the diamond saw notches had a smaller dislocation density in the vicinity of the notch as compared to those containing EDM notches. Based upon this investigation, the notches prepared by the diamond saw were adopted for fracture toughness testing in this study.
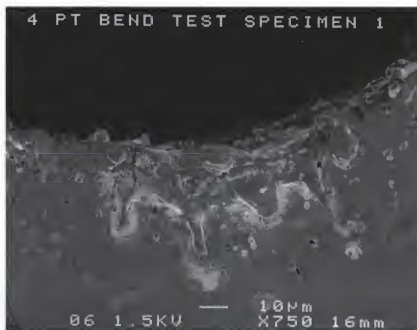
Figure A-1 A SEM micrograph showing the damage created by the EDM process of notch making.
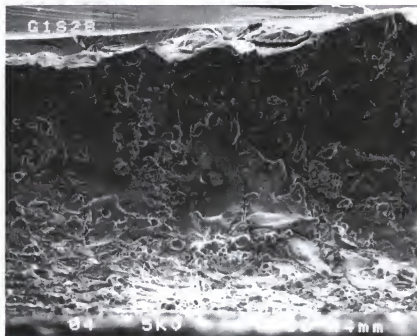
Figure A-2 A SEM micrograph showing the presence of micro-cracks ahead of the EDM notch.
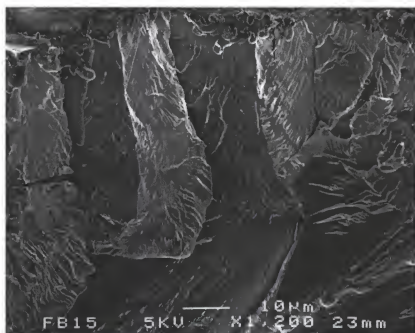
Figure A-3 A SEM fractograph showing the presence of facets of the size of EDM cracks on the fracture surface.
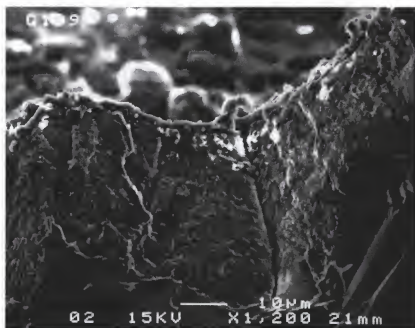
Figure A-4 SEM fractograph of a specimen which was heat treated in the notched condition showing the oxidation of the facets shown in Figure A-3.
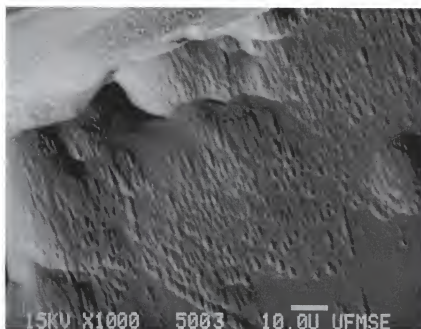
Figure A-5 SEM micrograph showing a high density of etch pits ahead of the notch prepared by the EDM.
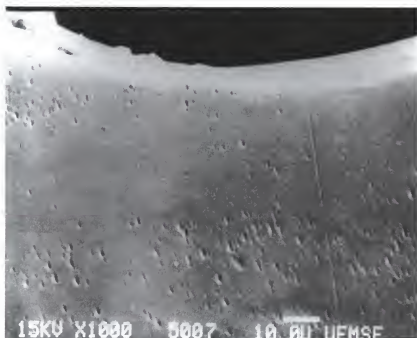
Figure A-6 SEM fractograph showing a low density of etch pits ahead of a notch prepared by the diamond saw.

APPENDIX B
DETERMINATION OF STRAIN HARDENING EXPONENT

Logarithmic of stress values were plotted against the logarithmic of strain in the region of uniform plastic deformation for tensile tests performed at different temperatures and strain rates. These plots are shown in Figures B1-B9. The best fit linear regression was obtained for each set of data and the slopes were determined. The linear curves indicate that these data obey the Holloman relationship, which is given by the following equation:

$$\sigma = K\varepsilon^n \qquad\qquad (B-1)$$

where σ is the stress, ε is the strain, K is the strength coefficient and n is the strain hardening exponent. Using these plots, The strain hardening exponent values were determined for each test condition and have been given in Table 4.6.
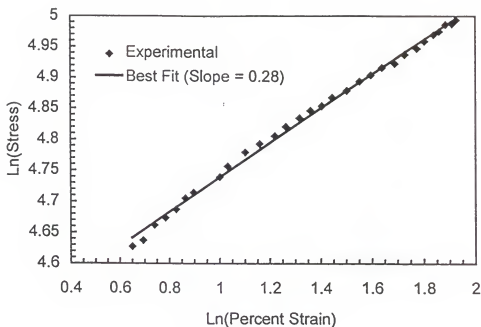
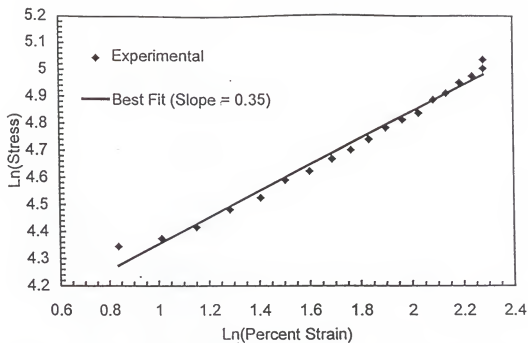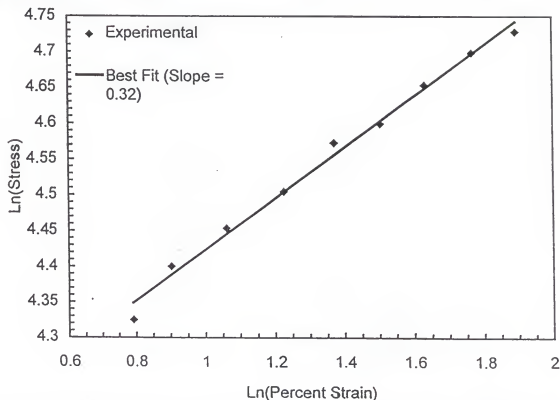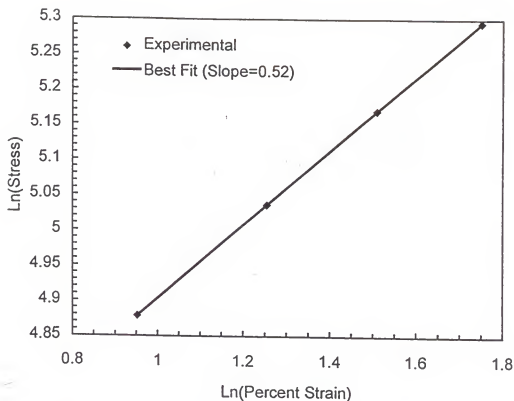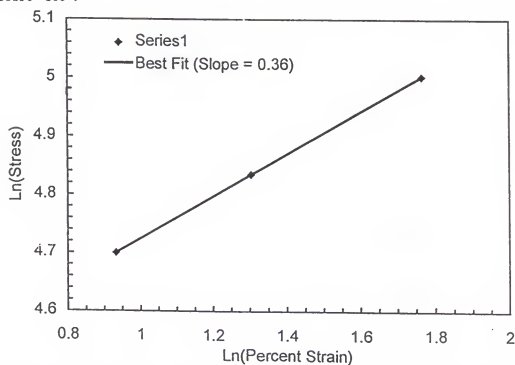Figure B-1 Determination of strain hardening exponent "n" at 20°C at a strain rate of 5×10^{-6} sec^{-1}.
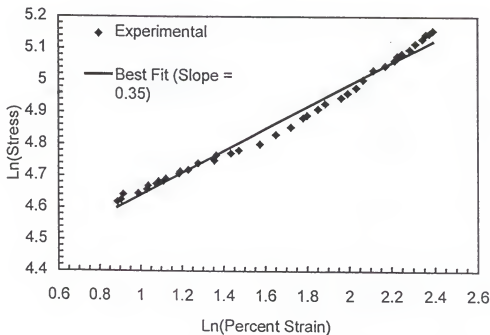
Figure B-2 Determination of strain hardening exponent "n" at 100°C at a strain rate of 5×10^{-6} sec^{-1}.
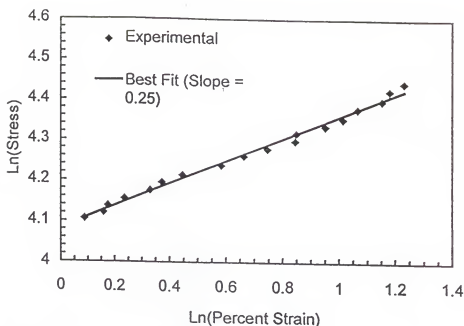
Figure B-3 Determination of strain hardening exponent "n" at 200°C at a strain rate of 5×10^{-6} sec^{-1}.
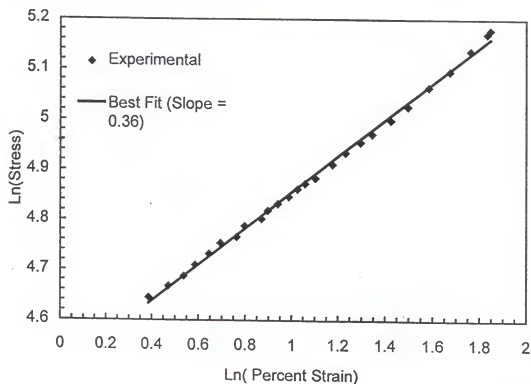
Figure B-4 Determination of strain hardening exponent "n" at 20°C at a strain rate of 5×10^{-5} sec^{-1}.

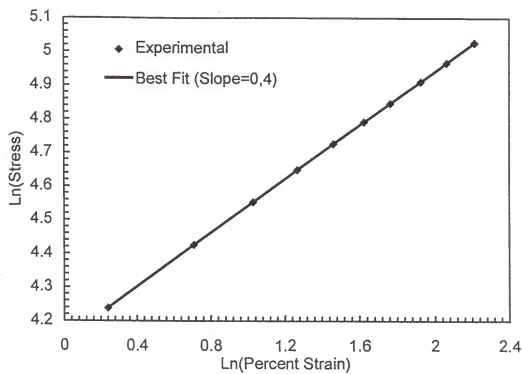Figure B-5 Determination of strain hardening exponent "n" at 100°C at a strain rate of 5×10^{-5} sec^{-1}.

Figure B-6 Determination of strain hardening exponent "n" at 200°C at a strain rate of 5×10^{-5} sec^{-1}.

Figure B-7 Determination of strain hardening exponent "n" at 20^0C at a strain rate of 5×10^{-3} sec^{-1}.

Figure B-8 Determination of strain hardening exponent "n" at 100^0C at a strain rate of 5×10^{-3} sec^{-1}.

Figure B-9 Determination of strain hardening exponent "n" at 200⁰C at a strain rate of 5×10^{-3} sec⁻¹.
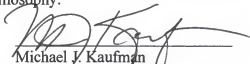
BIOGRAPHICAL SKETCH

Sanjay Shrivastava was born on June 26, 1967 in north-central India. He received a Bachelor of Engineering degree in metallurgical engineering from the University of Roorkee (India) in 1989 and a Master of Science degree in metallurgical engineering from the University of Nevada, Reno in 1991. Upon the completion of his master's degree, he worked at Ford Motor Company's Ford Research Laboratory in Dearborn, MI, during 1991-93 as a research engineer. He started pursuing a Ph.D. degree program at the University of Florida in the Fall of 1993. Recently, he has accepted an offer of employment from Ingersoll-Rand group of companies where he plans to work upon the completion of his Ph.D.

I certify that I have read this study and that in my opinion it conforms to acceptable standards of scholarly presentation and is fully adequate, in scope and quality, as a dissertation for the degree of Doctor of Philosophy.
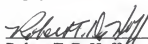
Fereshteh Ebrahimi, Chair
Associate Professor of Materials Science
and Engineering

I certify that I have read this study and that in my opinion it conforms to acceptable standards of scholarly presentation and is fully adequate, in scope and quality, as a dissertation for the degree of Doctor of Philosophy.
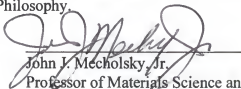
Michael J. Kaufman
Professor of Materials Science and
Engineering

I certify that I have read this study and that in my opinion it conforms to acceptable standards of scholarly presentation and is fully adequate, in scope and quality, as a dissertation for the degree of Doctor of Philosophy.

Robert T. DeHoff
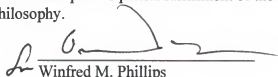Professor of Materials Science and
Engineering

I certify that I have read this study and that in my opinion it conforms to acceptable standards of scholarly presentation and is fully adequate, in scope and quality, as a dissertation for the degree of Doctor of Philosophy.

John J. Mecholsky, Jr.
Professor of Materials Science and
Engineering

I certify that I have read this study and that in my opinion it conforms to acceptable standards of scholarly presentation and is fully adequate, in scope and quality, as a dissertation for the degree of Doctor of Philosophy.

Bhavani Sankar
Professor of Aerospace Engineering,
Mechanics, and Engineering Science

This dissertation was submitted to the Graduate Faculty of the College of Engineering and to the Graduate School and was accepted as partial fulfillment of the requirements for the degree of Doctor of Philosophy.

May, 1997

Winfred M. Phillips
Dean, College of
Engineering

Dean, Graduate School